skb.se

SKB TR-25-06

ISSN 1404-0344
ID 2072060
August 2025

Analysis of copper samples from the canister in deposition hole 4 in the Prototype repository

Abdelkader Meroufel, Xuying Wang, Dan Persson, Alice Moya Nunez,
Kristina Lindgren, David Malmström, Rikard Norling
RISE AB

Summary

In the context of periodic assessment of durability of copper canisters exposed in repository-like environment in the Äspö Hard Rock Laboratory (HRL), an exhaustive characterization plan was implemented on six representative samples. Different techniques were combined with the aim to explore corrosion features (extent and chemistry), microstructure and possibly absorbed hydrogen quantification. The canister was part of the Prototype repository that started operation in 2001, and it was exposed for 23 years.

The results showed very limited extent of localized corrosion, which is in agreement with previous assessments of copper corrosion under similar conditions. This limited corrosion attack would develop during early post-closure phase of the canister deposition site where some residual oxygen is still present. From a microstructure perspective, the surface region near the corrosion layer showed a plastic deformation associated with grain refinement. The decrease in grain size supports the improved localized corrosion resistance. Further investigation would be needed for a better understanding of this possible relationship between copper canister surface machining and microstructure evolution. The canister surface chemistry showed variability including different compounds such as copper oxide (cuprite), chloride containing copper hydroxide (paratacamite), bentonite and some inorganic scale (gypsum and carbonates). The possibility of sulphur-based corrosion products was excluded when combining all characterization results together. The corrosion layer observed by cross-section analysis was thin (approximately 3 μm), discontinuous and appeared porous. Finally, the amount of absorbed hydrogen measured for two samples near the canister base showed a range between 0.4 to 2 ppm. The main source of the lower amount of hydrogen (sample 10) appears to be from the manufacturing process of the oxygen free pure copper. However, the source of the higher amount of hydrogen for sample 8 (~ 2 ppm) could not be ascertained and further investigation may be required for that.

Sammanfattning

För att utvärdera beständigheten av kopparkapslar exponerade i slutförvarsliknande miljö i Äspölaboratoriet (HRL) undersöktes sex representativa prover från Kapsel 4 i Prototypförvaret. Olika tekniker kombinerades i syfte att utvärdera korrosion (omfattning och kemi), mikrostruktur och eventuell absorption av väte. Prototypförvaret togs i drift 2001 och Kapsel 4 som återtogs 2024 har således exponerats för miljön i Äspölaboratoriet under 23 års tid.

Resultaten visade på en mycket begränsad omfattning av lokal korrosion, vilket är i överensstämmelse med tidigare resultat från Prototypförvaret och fältförsök under liknande förhållanden. Denna begränsade korrosionspåverkan härrör från den tidiga fasen efter tillslutningen av kapselns deponeringsplats då en del kvarvarande syre fortfarande är närvarande. Ur ett mikrostrukturperspektiv uppvisade området under den korroderade ytan en plastisk deformation associerad med kornförfining. Den minskade kornstorleken kan vara en förklaring till beständigheten mot lokal korrosion. Ytterligare studier skulle behövas för att förbättra förståelsen av denna möjliga koppling mellan kopparkapselns ytbearbetning och mikrostrukturutvecklingen. Kapselns ytkemi uppvisade variationer som inkluderar olika föreningar såsom kopparoxid (kuprit), koppar-hydroxo-klorid (paratakamit), bentonit och vissa oorganiska beläggningar (gips och karbonater). Möjligheten till förekomst av svavelbaserade korrosionsprodukter uteslöts när alla karakteriseringsresultat kombinerades. Korrosionsskiktet som observerades vid tvärsnittsanalys var tunt (ungefär 3 μm), diskontinuerligt och uppvisade viss porositet. Slutligen visade mängden absorberat väte uppmätt för två prover nära kapselbasen ett intervall från 0,4 till 2 ppm. Den huvudsakliga källan till den lägre mängden väte (prov 10) verkar vara från tillverkningsprocessen av den syrefria rena kopparn. Däremot kunde vätekällan för prov 8 (~2 ppm) inte fastställas och ytterligare undersökning krävs för att bättre förstå det resultatet.

Contents

1 Introduction

1.1 Background

Continuous safety assessments are conducted by SKB to ensure a long-term safe nuclear fuel spent repository that is planned to be built at Forsmark site in the municipality of Östhammar, Sweden (SKB 2011). Such assessment aims to respect applicable Swedish regulations and provide inputs for lifetime design of the whole structure. In 2022, the Swedish government allowed SKB to build a final repository based on the Environmental Act, while the evaluation according to the Nuclear Act continues in a stepwise process governed by the Swedish Radiation Safety Authority (SSM).

SKB's concept for a spent nuclear fuel repository is called KBS-3. Technically, this concept consists of copper canisters with a cast iron insert containing spent nuclear fuel. The whole metallic assembly is embedded in compact bentonite clay and deposited in deposition holes at approximately 500 m depth in granitic rock in contact with groundwater (Figure 1). The purpose is to isolate the nuclear waste from both environment and population as long as necessary.

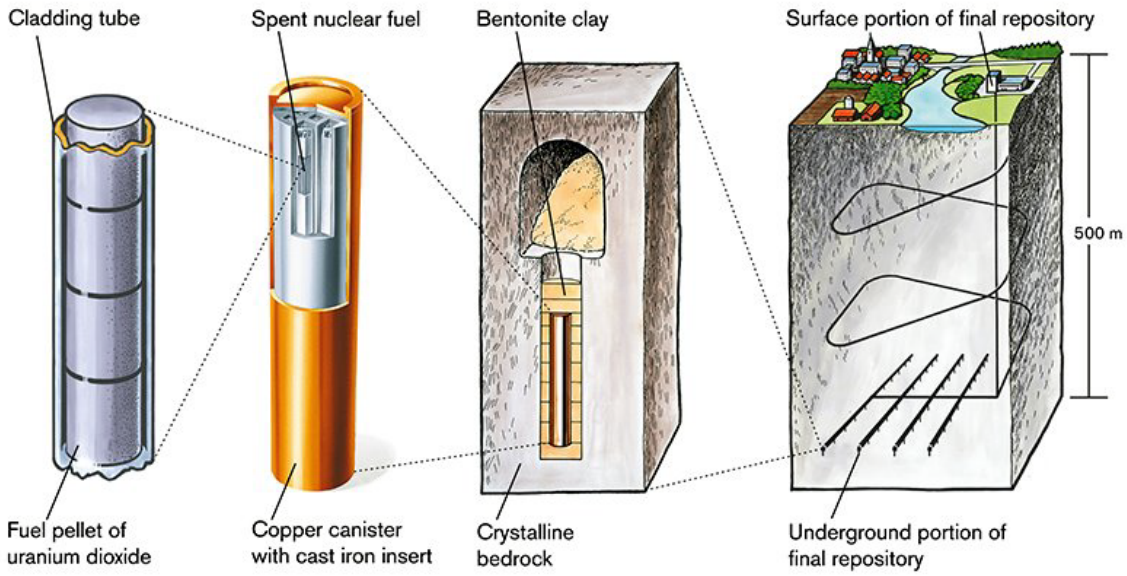

Figure 1. *The KBS-3 concept for management of spent nuclear fuel.*

In order to demonstrate capability of installation of the canister, buffer and backfill system, and to evaluate the performance of the clay system under repository conditions, a Prototype repository representing a full-scale field experiment was built in the Äspö Hard Rock Laboratory (Äspö HRL). The Prototype repository contained six deposition holes with full-scale copper canisters (supplied with heaters to mimic the thermal load from the spent nuclear fuel) surrounded by MX-80 bentonite buffer. The deposition tunnel was divided in two sections, sealed and separated with concrete plugs. The outer section contained two canisters and were retrieved in 2011 (Taxén et al. 2012, Taxén 2013), while the inner section contained four canisters retrieved during 2024–2025. The overall objective of the retrieval was to study the actual conditions of canister, buffer, backfill and the surrounding rock after being subjected to natural groundwater inflow and heating for a considerable time. The maximum temperature during the test period in standard conditions was about 90 °C. The chemical conditions are initially dominated by air filling the initial gap between the canister and buffer, and the pore space of the buffer clay, while on a longer timescale the conditions are determined primarily by the flux of groundwater responsible for wetting the bentonite buffer during the experiment (Johansson et al. 2020).

Different aspects of durability towards various loads were studied including chemical, microbiological, and mechanical loads. Among them, corrosion is a potential threat that can induce a loss of integrity of the canister, which could have serious impact on both the environment and population safety. An exhaustive state of the art was conducted by SKB (King et al. 2010) summarizing the different expected corrosion forms for copper canisters especially and corresponding environmental conditions including their evolution. The main conclusion of that report supports a life expectation exceeding 100000 years that was originally claimed in 1978 (Swedish Corrosion Institute and its reference group 1978). Even with pessimistic assumptions regarding detrimental phenomena, canister failure in one million years will be rare. Within this context, SKB continues to check the validity of such claim through field experiments on representative canister exposed to the same corrosive environment in the absence of nuclear radiation. The most recent assessments of canister integrity and post-closure safety of the spent fuel repository can be found in SKB (SKB2019, 2022a, 2022b).

In the examination of previous field tests, different characterization techniques have been adopted for tracking any possible localized corrosion, hydrogen absorption, and intergranular attack. Examination of copper corrosion in field tests have been published as SKB reports, including exposure durations reaching up to 20 years (Taxén et al. 2012, Taxén 2013, Johansson et al. 2020).

The major findings of those assessments highlighted the presence of thin copper oxide and copper hydroxycarbonate layers mixed with bentonite elements and a very minor localized corrosion attack which did not exceed 10 μm. For hydrogen absorption, there were no evidence of such process since the quantified amount remained in the range of 0.4 ppm. Moreover, the microstructure features did not support any possibility of intergranular or stress corrosion cracking risks. In the present report, the aims are to identify corrosion products and quantify any type of localised corrosion, hydrogen uptake, and to examine the microstructure near the corroded surface. However, compared with the examination of canisters from the outer section of the Prototype repository, some additional and modified aspects are considered for the characterization methods. This includes the consideration of surface topography by 3D optical surface scanning, μ-Raman spectroscopy and analysis of microstructure features near the corroded surface.

1.2 Objectives

The present work is conducted using a combined fundamental and applied multi-analytical approach to meet the following objectives:

- Characterise the outer canister sample surfaces in terms of corrosion products and surface profile/defects.
- Characterise the corrosion layer (continuity, chemistry, thickness) and its possible role in the corrosion mechanism.
- Determine any localized corrosion attack extent (depth).
- Assess the amount of possible absorbed hydrogen, its vertical profile (i.e. through the canister wall thickness) and possible contributing microstructural features.
- Discuss the dominant corrosion mechanisms.

2 Materials and methods

2.1 Materials

SKB extracted samples from the canister (Figure 2) by drilling out cores through the wall thickness and then delivered these samples to RISE lab for analysis. The inner section of the repository from where the canister was extracted is in service since 2001 (23 years).

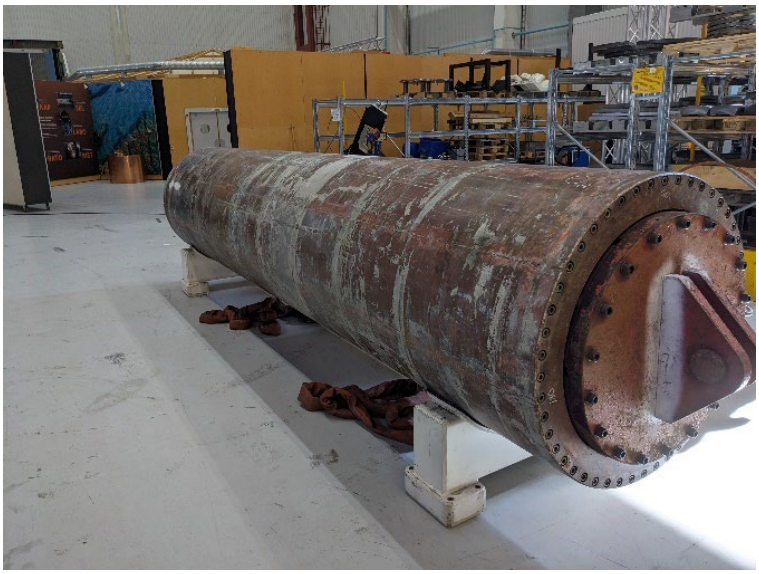

Figure 2. *Copper canister from which exposed samples were obtained.*

Samples´ locations in the canister were communicated by SKB and summarized in Table 1.

Table 1. Copper canister samples´ locations

Sample number	Circumferential position (°)	Distance from canister base (m)
1	3	4.57
4	160	2.07
6	5	1.22
8	15	0.06
9	5	3.89
10	65	0.75

Upon arrival at RISE, six extracted samples (exposed to compacted bentonite) from the canister and one reference copper sample (obtained from SKBs canister lab), in the form of cylinders (drill cores), were unpacked and documented with photography (Figure 3). The samples´ dimensions are summarized in Table 2. All received samples were stored before and after analysis in controlled environment chamber with continuous N2 gas flow to minimize surface oxidation. It can be noticed that the outer (exposed to bentonite) surface of the canister was machined giving the observed lined pattern surface.

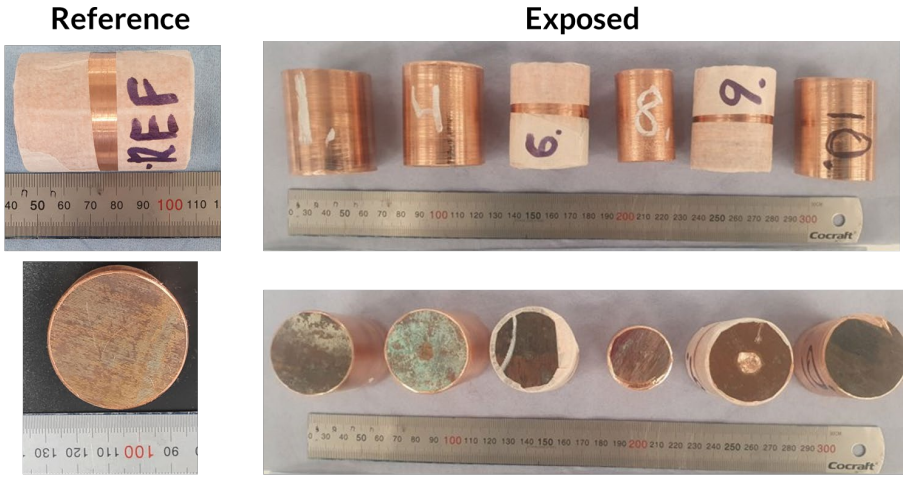

Figure 3. *Overview pictures (from side and top view) of six exposed samples (to bentonite) and one non-exposed reference sample.*

Table 2. Dimensions of copper samples including their outer diameter (O.D) and height (H)

Sample	REF	1	4	6	8	9	10
O.D (mm)	38.8	38.8	38.8	38.8	30	39.14	38.8
H (mm)	54.5	47	47	47	45	48	50

As the canister has already been removed from the exposure site, the effects of exposure to atmosphere shall be considered when interpreting the results. The canister is made of oxygen free pure copper material with typical composition indicated in Table 3.

Table 3. Copper canister material composition (SKB, 2010)

Element	Cu	P	O	S	Ag	Fe	H
Content[1]	99.99	68.4	1.13	4.77	13.8	1.06	0.37
SD[2]	0.001	7.8	0.49	0.47	0.7	0.44	0.14

[1] Mean values in ppm apart for copper which is in wt.%
[2] Standard deviation

2.2 Methods

To determine the extent of corrosion attack and related features after exposure, an examination plan was defined, discussed and approved by SKB representative. It consists of a series of characterization techniques, which were adopted following an order defined by their purpose, nature (destructive or non-destructive to the exposed surface), complementarity and related sample preparation requirements (Figure 4).

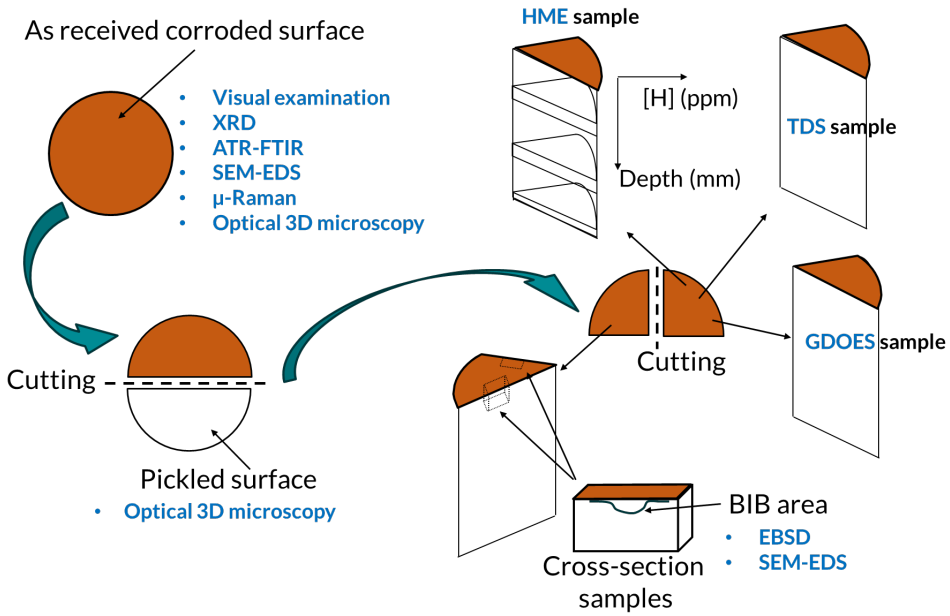

Figure 4. *Examination plan conducted on exposed copper samples.*

Once the visual inspection was completed, the surface chemistry techniques (SEM-EDS, XRD, µ-Raman and ATR-FTIR) were carried out on selected sites on the exposed surfaces of the samples to obtain data on the most relevant features. µ-Raman spectroscopy was conducted only for one sample (sample #10).

3D optical surface scanning was then carried out on the whole surface, while keeping surface products in place. Then, the samples were dry cut (to avoid any contamination from the cooling fluid) in half along the axis, resulting in two parts for each original sample (Figure 4). The cutting parameters include a wheel speed of 1200 rpm and wheel feed speed 0.009 mm/s. Those parameters were inspired from a research work (Tefera et al. 2023) where the authors optimized the cutting parameters to control the surface roughness for different copper alloys containing Cr and Zr. Part of the surface was further scanned after chemical pickling. Pickling for the removal of surface products was conducted on half of the surface using 0.5 M sulfamic acid (50 g of sulfamic acid per 1000 mL of distilled water) without adverse effects on the base metal based on previous similar work (Johansson et al. 2020).

The other non-pickled part was further cut into two pieces. For all the exposed samples one of these pieces was prepared for cross sectional analysis. During this step, two areas on each sample were selected for BIB[3] preparation before being analysed in the SEM for corrosion/surface layer features, localised corrosion attack, and microstructure features (EBSD[4]). Another cut piece was used for element distribution analysis near the surface by means of GDOES[5]. Additionally, one piece from a sample of interest was prepared for Hot Melting extraction (HME) and Thermal desorption spectroscopy (TDS) analyses, giving a profile of total hydrogen content through the wall thickness of the canister and diffusible hydrogen content respectively.

[3] Broad ion beam
[4] Electron backscatter diffraction
[5] Glow discharge optical emission spectroscopy

Careful handling of the samples was considered during all phases of the work to avoid the disturbance of the exposed surface and nearby microstructure. This includes the optimisation of cutting conditions, working in clean environment and minimisation of sample handling. More details about the different techniques can be found below.

An inventory gathering samples and their corresponding analysis methods is summarized in Table 4. Samples 8 and 10 were selected by SKB based on their black appearance suspecting the presence of sulphur-based corrosion product associated with hydrogen reduction reaction that would promote hydrogen absorption.

Table 4. Summary of copper samples and employed analysis methods

Sample ID	Analysis methods							
	SEM/EDS surface	SEM/EDS/EBSD cross-section	XRD	FTIR	3D surface	GDOES	TDS	HME
REF	-	-	-	-	X	-	X	X
#1	X	X	X	X	X	X	-	-
#4	X	X	X	X	X	X	-	-
#6	X	X	X	X	X	X	-	-
#8	X	X	X	X	X	-	X	X
#9	X	X	X	X	X	X	-	-
#10	X	X	X	X	X	X	X	X

2.2.1 Metallography

Microstructure features of the copper used for canister manufacturing were examined only for the reference copper sample on the cross-section surface using a Leica light optical microscope (LOM) with different magnifications. Sample preparation included grinding with SiC paper grit P600, P1200, P2500 and P4000, followed by polishing with diamond paste from 3 µm down to 0.25 µm. The surface was rinsed with ethanol after each step and ultrasonically cleaned in distilled water for 5 min in the last step. The polished specimen was etched to make the microstructure visible. The etching method was following the standard ASTM E407-07, using No. 26 reagent (5 g $FeCl_3$, 10 mL HCl, 50 mL glycerol, and 30 mL water) at room temperature for 5 s (ASTM E407 07). Thereafter, the sample was rinsed with distilled water and ethanol to remove the remaining etchant on the surface.

2.2.2 Scanning electron microscopy (SEM)

To investigate both surface and cross-section corrosion layer in terms of morphology and related chemical information, all exposed samples were characterized using a Zeiss Sigma 3000VP scanning electron microscope (SEM) equipped with an Oxford Instruments X-maxN energy dispersive X-ray spectroscopy (EDS) detector. The SEM operated with an electron beam voltage of 15 keV and a current of about 1–2 nA, utilizing a Secondary Electron (SE) detector to image the specimen surfaces. The SEM and EDS analyses were conducted using SmartSEM and AZtec software, respectively. Carbon was deconvoluted from the spectra, as it was assumed to be completely or partially a contaminant from the sample or chamber. The EDS analyses are known to be semi-quantitative.

Dry cut cross-section samples were mounted in epoxy resin before being subject to slight grinding and BIB surface preparation. BIB method with some optimization of its parameters offers high surface quality necessary for both SEM-EDS and EBSD analysis. BIB parameters consist in voltage of 6 kV (intermittent beam 60 s ON, 30 s OFF, 5 h + 4 kV 2 h) to get a larger surface necessary for proper EBSD analysis.

2.2.3 Glow discharge optical emission spectroscopy (GDOES)

The samples were analysed for element content by using a LECO GDS 850A glow discharge technique from LECO Corporation (St. Joseph, Michigan, USA). A circular area of 4 mm in diameter is continuously being sputtered in a small argon plasma (glow discharge). The optical emission coming from the various elements in the sample is then registered with an optical spectrometer - giving the elemental composition. Calibration has been done using reference samples (RM[6] and CRM[7]) with a known composition and content. Examples of used certified reference samples are steel samples from Jernkontoret (JK) and samples from the American National Institute of Standards and Technology, NIST. The GDOES could be equipped with either a DC or RF lamp, and in this case the samples were analysed using the DC-lamp due to its stability and performance.

For the GDOES source settings the control mode was set to current (30 mA) and the pressure control to voltage (700 V). The startup pressure was set to 7.0 torr. The instrument was drifted (i.e. corrected calibration) against the certified references NIST C1253, BNF C09.05, MN4 and CP3 from the Institute of non-ferrous metals, the brass reference 2161-5x and a piece of pure copper.

The sputtering rate is well known by calibrations against reference materials (RM, CRM), normally around 20–100 nm/s. The results are given as a weight-percentage curve plotted against sputtered depth. This feature makes GDOES therefore neat by being able to quickly measure thickness and elemental composition of thin films. The analysis gives an average value of the film thickness and elemental composition over the sputtered area, with the smallest information depth of around 1 nm.

The GDOES samples were cut using a band saw and cooled with ethanol to reduce the heat. No other sample pre-treatment was performed (Figure 5).

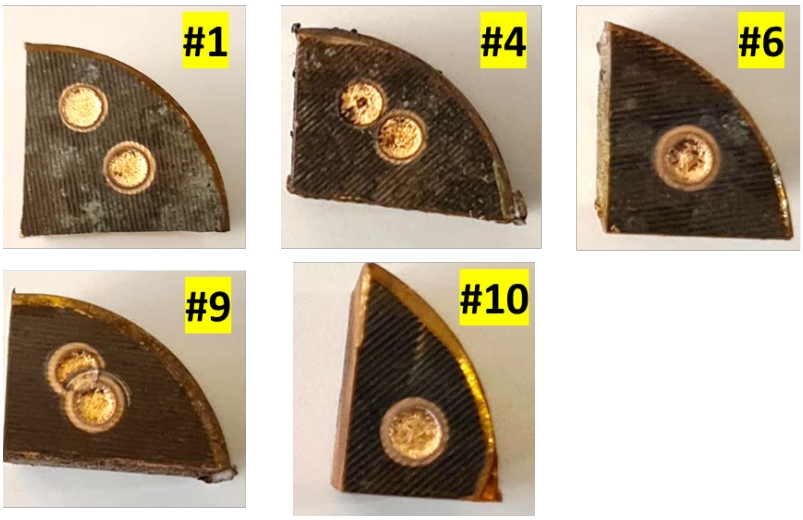

Figure 5. *GDOES samples and spot locations on the exposed surfaces.*

2.2.4 X-Ray Diffraction (XRD)

The X-ray diffraction (XRD) analyses were performed to identify surface products with crystalline structure, by using a Bruker D8 Discover instrument. The data was collected between 4 and 110° (2θ) with a copper anode having a K_α wavelength of 1.5418 Å. A Ni filter was used to reduce the intensity of the Cu K_β X-rays. The XRD beam size is about 10 mm^2 considered the averaging over large surface area. For compounds identification, the Crystallographic Open Database (COD) available in the DIFFRAC.EVA software was used.

[6] Reference material
[7] Certified reference material

2.2.5 Fourier Transform Infra-Red (FTIR) spectroscopy

FTIR in attenuated reflection transmission (ATR) mode is a qualitative technique which allows for determination mainly of both amorphous and organic based surface compounds due to their strong IR absorption, but also oxides and other inorganic products. Measurements were performed in a Vertex 70 spectrophotometer with a Specac Quest ATR accessory, using a diamond internal reflection element (IRE) at an incident angle of 45˚. Spectra in the approximate region 450 to 5400 cm^{-1} were acquired at resolution of 8 cm^{-1} and around 256 scans for both background and samples. ATR-FTIR analyzed area is 1–3 mm^2. Literature and functional group absorbance bands tables (RRUFF, NIST) were considered for the band's assignments/attributions. FTIR is challenging to ascertain alone the compounds identification.

2.2.6 µ-Raman spectroscopy

µ-Raman spectroscopy provides complementary information to both FTIR and XRD with better lateral resolution. A WITec Alpha 300 RAS system equipped with a 532 nm excitation laser was used to carry out the measurements. The 50x ZEISS LD EC Epiplan-Neofluar objective was used. Due to the high surface roughness, a 50x objective was selected. Raman spectra were obtained on a zone of 1–2 µm in diameter and the analysis depth can go up to 10 µm. The measurements were carried out using a grating of 1800 gr/mm to obtain high spectra resolution better than 0.5 cm^{-1}. The obtained results are subject to peaks identification through Witec® software which include established database such as RRUFF.

2.2.7 Surface topography

The surface profile and topography were characterized using an Alicona InfiniteFocusSL 3D optical microscope profilometer based on focus-variation. A 5x magnification objective lens was used to scan the entire surface of the Cu samples with vertical and lateral resolution of 0.5 µm and 10 µm, respectively. The 3D topography data was further processed using Mountains Map 9 image processing software. Minimal post-measurement processing was performed and included image cropping and form correction. Two types of roughness were determined i.e. surface roughness of the entire sample surface and random line profile. For surface roughness, ISO 25187 standard was applied where the deepest and the highest point were detected through the surface scanning. Line roughness estimation was done based on ISO 4287 guidelines. Additionally, pitting characterization under surface products at selected local area of sample #4 was performed using three different magnifications (5x, 20x and 50x).

2.2.8 Thermal desorption spectroscopy (TDS)

In this work a TD-MS instrument consists of IR07 for TDS-measurements from Bruker Ltd used in combination with a mass spectrometer from InProcess Instrument GmbH for detection. Nitrogen was used as the carrier gas and hydrogen gas was used as the main means of calibrating the instrument for hydrogen measurements. All gases were of instrument quality (Linde gas > 99.999 % purity). Gas calibration was performed with undiluted hydrogen gas. Furthermore, a reference material produced by LECO Corporation, i.e., steel metal samples with a specified hydrogen content and standard variation (3.5 ±0.6 and 6.7 ±0.6 ppm) was used for verification. Temperature interval was between 30 and 800 °C with a heating rate of 1 °C/s.

2.2.9 Hot Melt Extraction (HME)

Galileo G8 instrument for the determination of bulk hydrogen in copper was used for total hydrogen content measurement. Melt-extraction is the conventional method of measuring hydrogen and is based on samples (of approx. 1 g) that are melted in a flow-through graphite crucible under Ar atmosphere. The light elements are removed as gases and after purification of the gas mixture of CO, CO_2, H_2O, N_2, etc. hydrogen is detected by its effect on the thermal conductivity of Ar/H_2 mixture. This method can be very sensitive, and the instrument is capable of an accuracy of about 0.1 ppm. Calibration is done with steel reference samples with known concentrations (3.5 ±0.6 and 6.7 ±0.6 ppm) provided by Leco. Figure 6 shows the sample preparation for both TDS and HME analysis. Both TDS and HME samples preparation includes cutting under pure ethanol cooling.

The sensitivity of the obtained total H content by HME to the surface conditions of the samples was highlighted in previous assessments where surface deposits (e.g. bentonite particles) were found to have a considerably higher H content than the bulk material (Granfors 2017). This aspect was not investigated in the present characterization due to the limitation of samples and the analysis included the surface layer which was not removed.

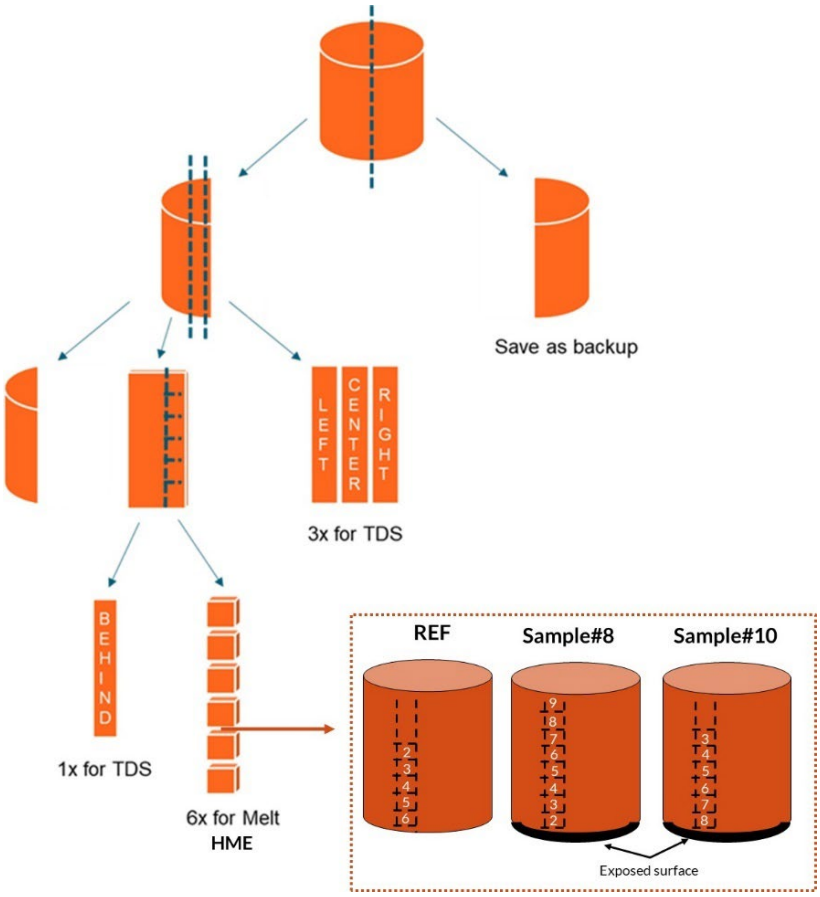

Figure 6. *Sample preparation for hydrogen content analysis by TDS and HME.*

3 Results

3.1 Appearance of samples in as-received condition

All received copper samples were removed from vacuum bags and wrapping paper respectively and then inspected and photographed. Figure 7 shows the surface images of drill core of one reference and six exposed samples.

The surface displayed considerable variation, largely consisting of a combination of dark black, white, green and red surfaces. In some regions, metallic shiny surface with typical copper colour was observed. Surface machining striations were observed and are expected to be related to the canister manufacturing stage

Evidence of mechanical damage was observed for certain samples (either in the core or the edge) which can be due to sampling and/or handling procedures as for samples #4, #6, #8, #9 and #10.

Solid corrosion products and probably bentonite residues are visible with variable appearance on the surface, compared with the reference sample. Samples #1 and #4 surfaces distinguish from the others by their colour, texture and flaking which may indicate thicker surface layer. Unexpected surface redness was detected on samples #1 and #8. The presence of white line on sample #6 is caused by marking during sampling as confirmed by SKB engineer. In general, all surfaces exhibited a non-uniform appearance when it comes to surface products coverage. Also, it is not obvious to correlate the visual appearance to the sample´s locations in the absence of surrounding environment information.

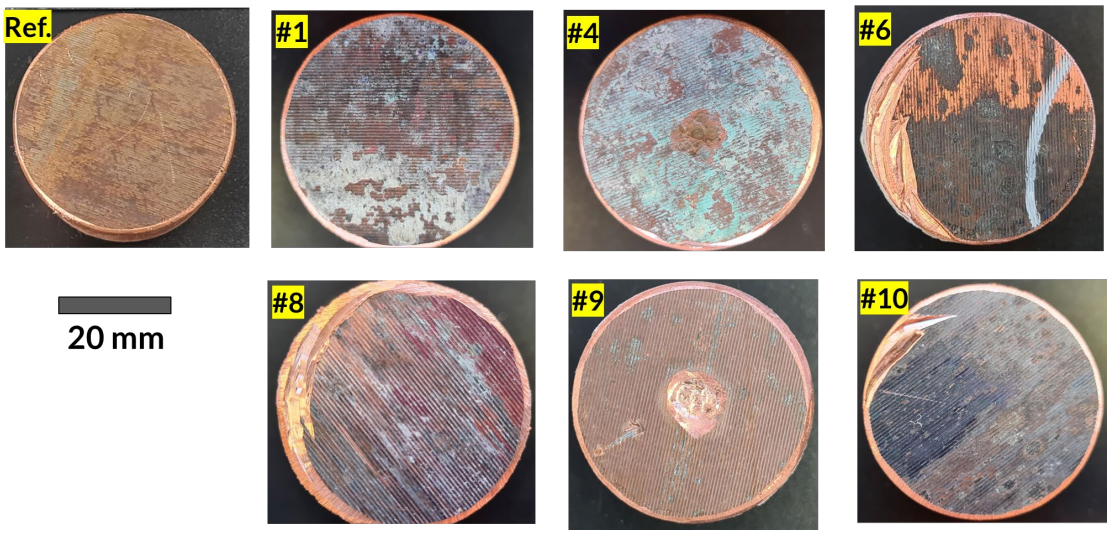

Figure 7. *Visual appearance of samples surfaces including the non-exposed reference sample (Ref.) and six exposed samples (noted #1, #4, #6, # 8, #9, #10).*

3.2 Metallography

Reference copper sample was subject to microstructure examination where its surface was finely polished and lightly etched according to procedure described in section 2.2. The images were taken from three different sites under a microscope with 50x and 200x magnification, as shown in Figure 8. It can be seen in that copper sample is composed of grains with sizes ranging from 30 µm to 300 µm, with irregular polygon structures. This structure also includes a high fraction of twinned grains as observed in previous assessment (Taxén et al. 2012)

Dark spots are observed at grains and grain boundaries which may be related to the surface preparation and/or to some microporosity. Diamond suspension particles can be embedded easily on the soft copper surface depending on polishing force, diamond particles size, and other factors. Also, microporosity of pure copper is believed to originate from the manufacturing stage because of trapped hydrogen in the melt (Sunny group 2023, Bodington 2024). Hydrogen trapping in copper is preferentially in grain boundaries but can also be in the bulk lattice (in case of defects such as dislocations or vacancies) (Nagumo et al. 2023). Deeper investigation of this aspect is out of the scope of the present analysis.

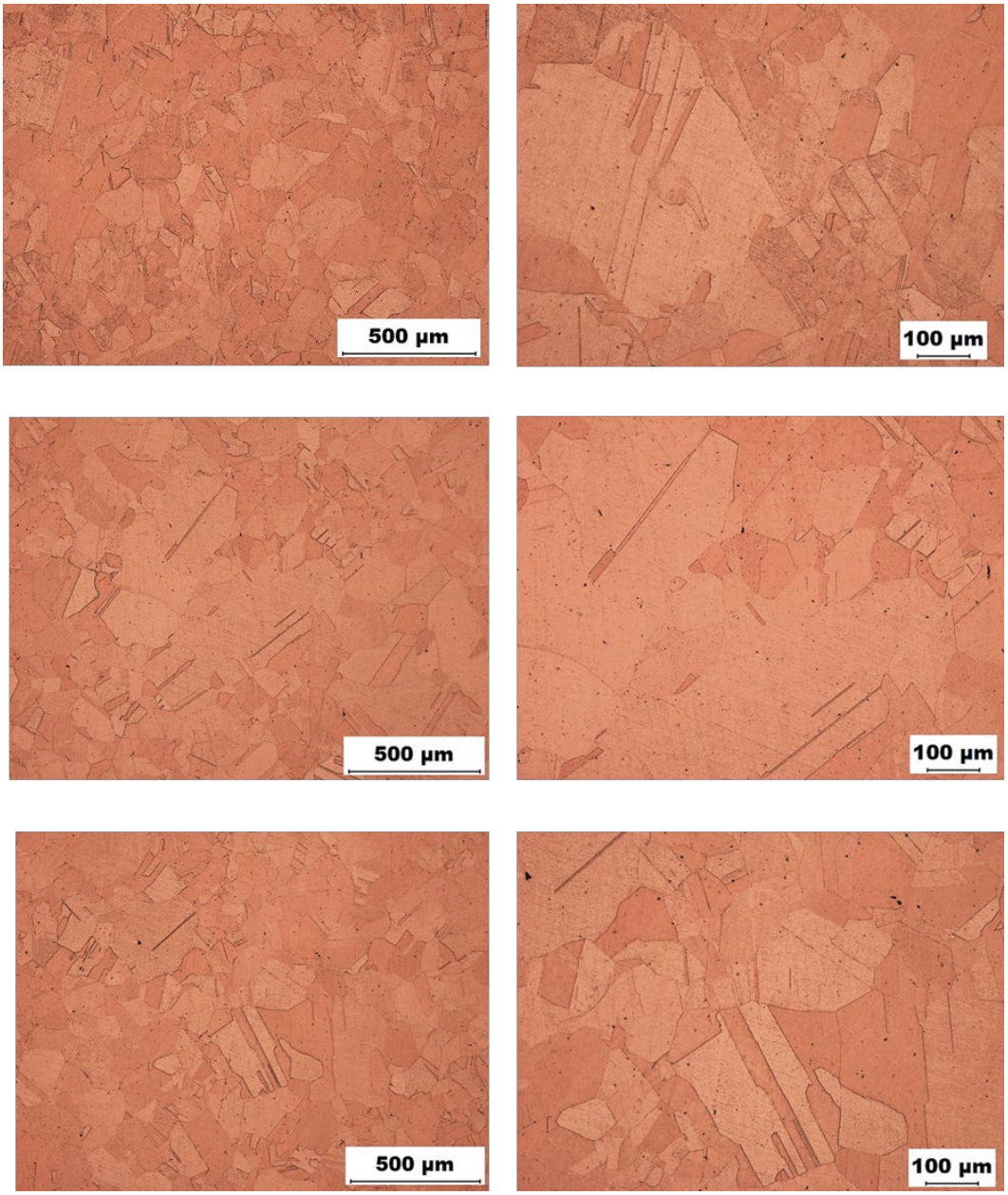

Figure 8. *Metallographic microstructure of the reference copper sample.*

3.3 Corrosion products

3.3.1 SEM/EDS

SEM/EDS analysis was conducted on different sites of the surface selected based on their different features (colours), as shown in Figures 9 to 14. When feasible, each distinct surface colour was subjected to individual measurements.

SEM images revealed microscopic details of the machining striations observed visually (section 3.1) and the patchy character of surface products. The images depicted light grey areas, which appear to be bare copper surfaces with a thin oxide layer, while darker areas with bright white are attributed to corrosion products and some surface deposits (probably bentonite). The white regions could result from the charging effect of the non-conductive bentonite which is more significant for thicker locations.

EDS elemental analysis was performed on each site (area analysis) to determine its average elemental composition. The summary of all detected elements is presented in Table 5. For most of samples, surface elements consisted of Cu and O, with variable content of other elements such as Mg, Na, Al, Si, K, Ca, Fe and Ti. Those elements are expected to come from bentonite and or groundwater (Jönsson et al. 2009). Additionally, small amounts of Cl and S were observed, particularly in samples #4, #6, #8, #10, as shown in Figures 10, 11,12, and 14 respectively. The sulphur content varied between samples and reached some significant levels in some locations i.e. 10 at. % and 15 at. % for samples #6 and #10 respectively. Different possible sources can be mentioned for this element including groundwater, corrosion products, or bentonite. Moreover, an additional probable source would be MoS_2 compound which is part of a lubricant (Molykote®) used for rings during manufacturing phase (Taxén et al. 2012). A spot analysis on sample #10 showed an amount of 13 at. % S and 4 at. % Mo (see Appendix A-Figure A-1). However, the simultaneous identification and exact quantification of both S and Mo is difficult because of peak overlap in the EDS spectra making the results only indicative of the elements coexistence. Further, elemental analysis also showed unrealistically high levels of F element on some locations from sample #10 surface, which can be missleading considering that F is difficult to quantify by EDS due to its low atomic number and possible peak overlapping with iron element (Shindo et al. 2002). This element was not detected on canister surface in previous assessment while it can exist in the groundwater with concentration not exceeding 2.6 ppm (Olofson 2023). However, in our case the high amount could not be considered due to the absence of this element on other characterization techniques.

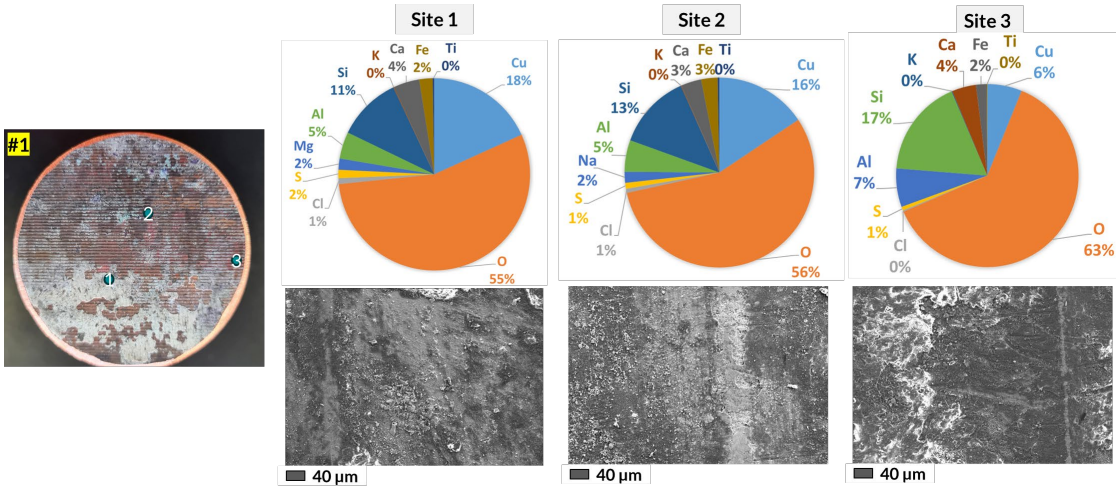

Figure 9. *SEM images of analyzed area and corresponding average elemental composition (at. %) by EDS mapping of sample #1 for three different sites.*

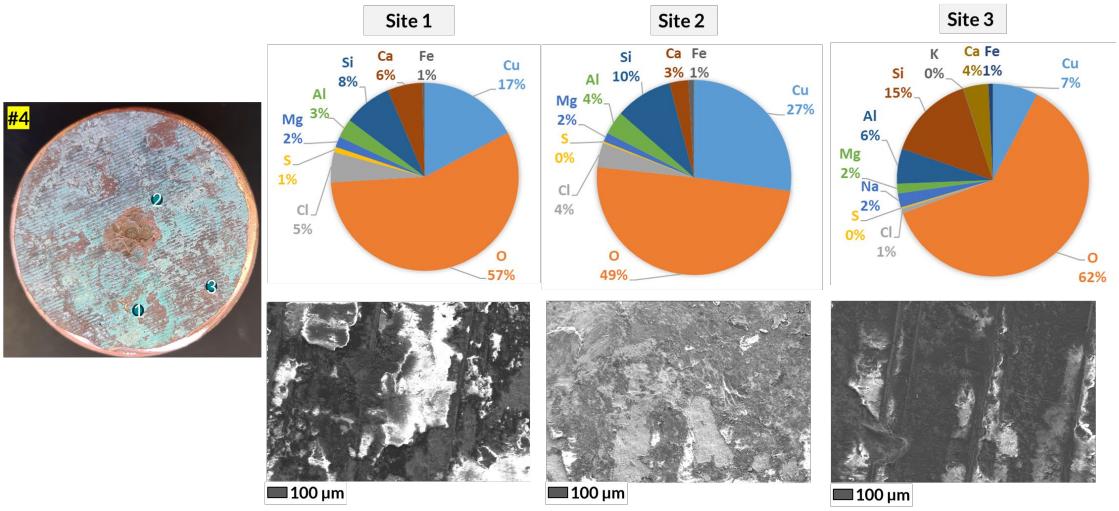

Figure 10. *SEM images of analyzed area and corresponding average elemental composition (at. %) by EDS mapping of sample #4 for three different sites.*

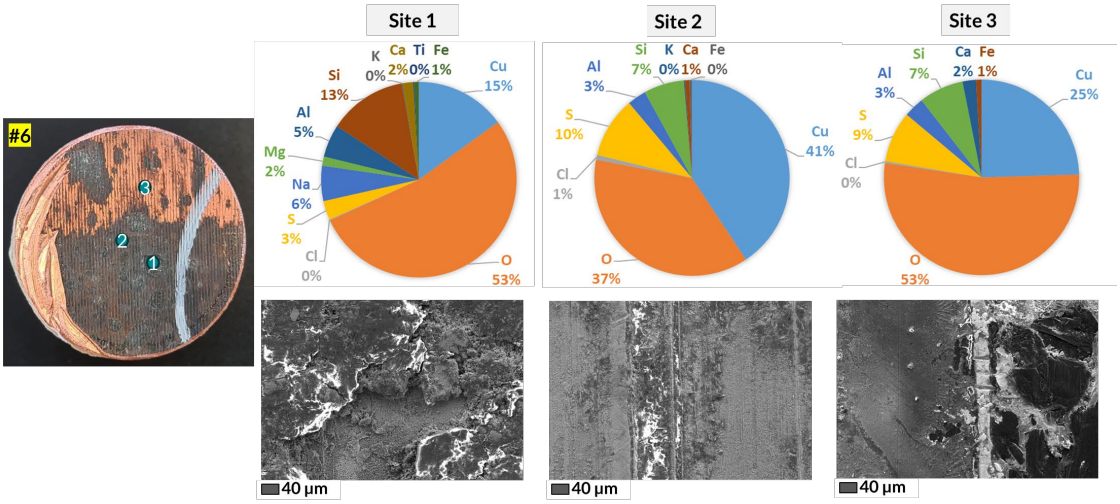

Figure 11. *SEM images of analyzed area and corresponding average elemental composition (at. %) by EDS mapping of sample #6 for three different sites.*

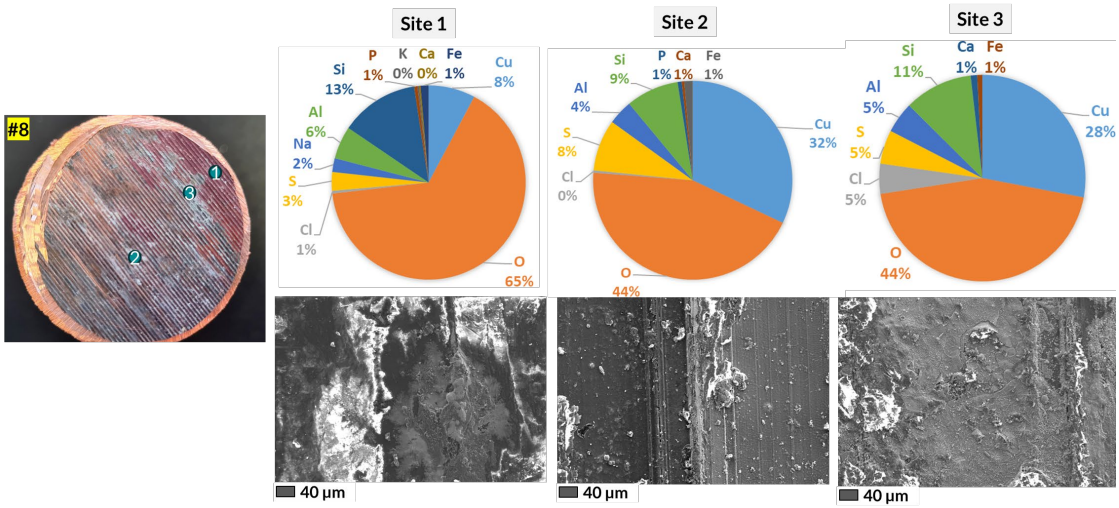

Figure 12. *SEM images of analyzed area and corresponding average elemental composition (at. %) by EDS mapping of sample #8 for three different sites.*

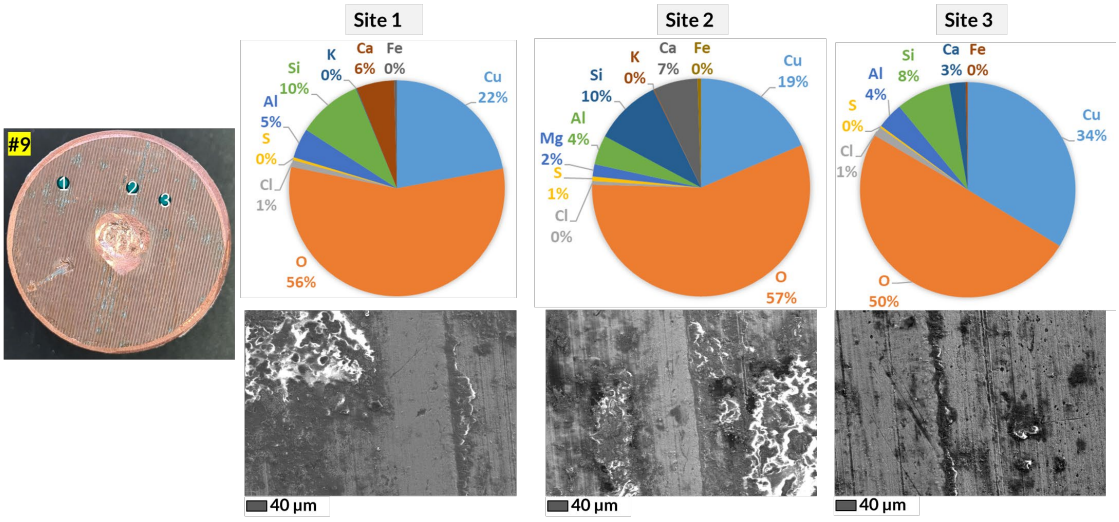

Figure 13. *SEM images of analyzed area and corresponding average elemental composition (at. %) by EDS mapping of sample #9 for three different sites.*

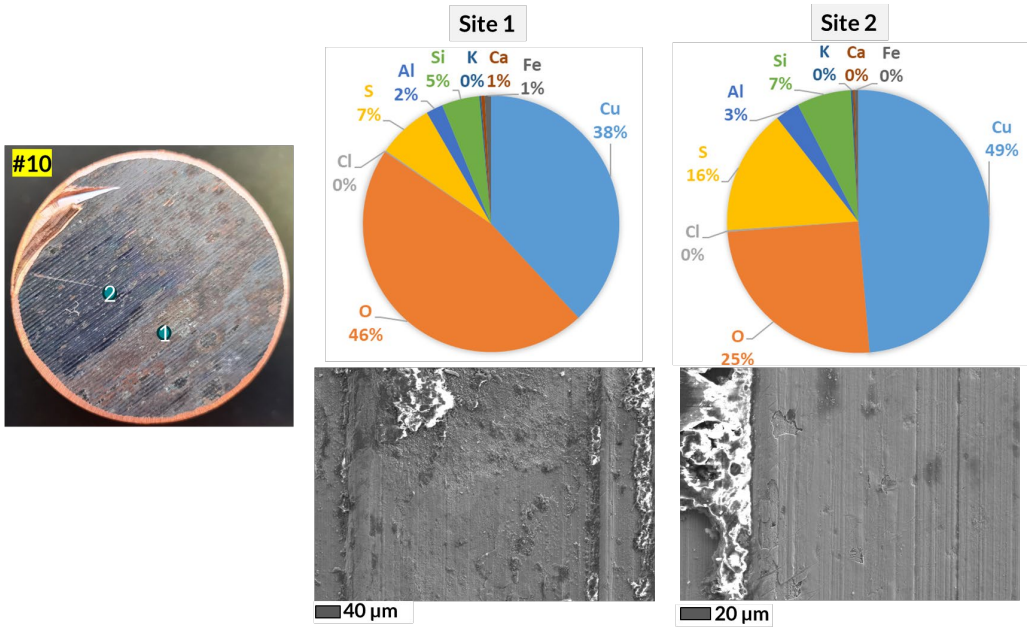

Figure 14. *SEM images of analyzed area and corresponding average elemental composition (at. %) by EDS mapping of sample #10 for two different sites.*

Table 5. Summary of elemental analysis by EDS for all samples (in at. %)

Sample	Site	Element (at. %)												
		Cu	O	Cl	S	Mg	Na	Al	Si	K	Ca	Fe	Ti	P
1	1	18.22	55.06	0.98	1.4	1.88		4.5	10.82	0.12	4.38	2.24	0.26	-
	2	15.62	55.86	0.69	1.01	-	1.87	5.38	12.8	0.11	3.47	2.79	0.29	-
	3	6.14	62.41	0.23	0.67	-		6.81	17.33	0.13	4.28	1.89	0.11	-
4	1	17.25	56.78	5.21	0.91	1.83	-	3.28	8.32	-	6.01	0.41	-	-
	2	27.25	49.46	4.05	0.29	1.48	-	3.86	9.52	-	3.16	0.93	-	-
	3	7.62	61.75	0.78	0.24	1.63	2.37	5.89	14.63	0.1	4.23	0.75	-	-
6	1	14.99	53.18	0.15	3.15	1.51	5.83	5.4	12.99	0.17	1.7	0.77	0.16	-
	2	40.69	37.29	0.8	10.08	-	-	3.12	6.68	0.18	0.75	0.41	-	-
	3	24.53	52.81	0.3	8.45	-	-	3.37	7.4	-	2.26	0.87	-	-
8	1	7.79	65.39	0.45	3.11	-	2.29	5.45	13.1	0.26	0.25	1.33	-	0.57
	2	32.05	44.17	0.38	8.38	-	-	4.01	8.57	-	0.41	1.37	-	0.66
	3	28	44.55	4.71	5.3	-	-	4.87	10.75	-	1.03	0.79	-	-
9	1	22.06	56.13	1.03	0.42	-	-	4.46	9.67	0.11	5.69	0.42	-	-
	2	18.65	56.77	0.54	0.67	1.81	-	4.36	9.96	0.13	6.59	0.53	-	-
	3	33.74	49.69	1.4	0.28	-	-	3.94	8.17	-	2.46	0.32	-	-
10	1	38.07	46.41	0.18	6.99	-	-	2.13	4.75	0.21	0.46	0.8	-	-
	2	48.62	25.1	0.22	15.46	-	-	2.99	6.71	0.23	0.25	0.42	-	-

3.3.2 GDOES

Elemental depth profile was characterized by GDOES where the obtained spectra are shown in Figure 15 with one or two spots for each sample. Sample 8 is not included since the available part was dedicated for an additional hydrogen analysis. It can be noticed from the penetration depth variation for each sample that there is an inhomogeneity of the sample. The detected elements remain like what was found by EDS analysis. Due to the non-availability of reference samples for calibration, both chlorides and hydrogen element are excluded from the results shown in Figure 15. The dominant elements are oxygen, silicon, aluminium and magnesium which decreased with depth increase in the same sample. The concentration of elements (except copper and oxygen) falls below 1 wt.% beyond 5 to 10 μm depths. The sulphur amount varies across and between samples which indicates its discontinuity. Relative to the sample position versus the canister base, both oxygen and sulphur amounts did not follow clear trends. Further discussion is given in section 4 (Discussion).

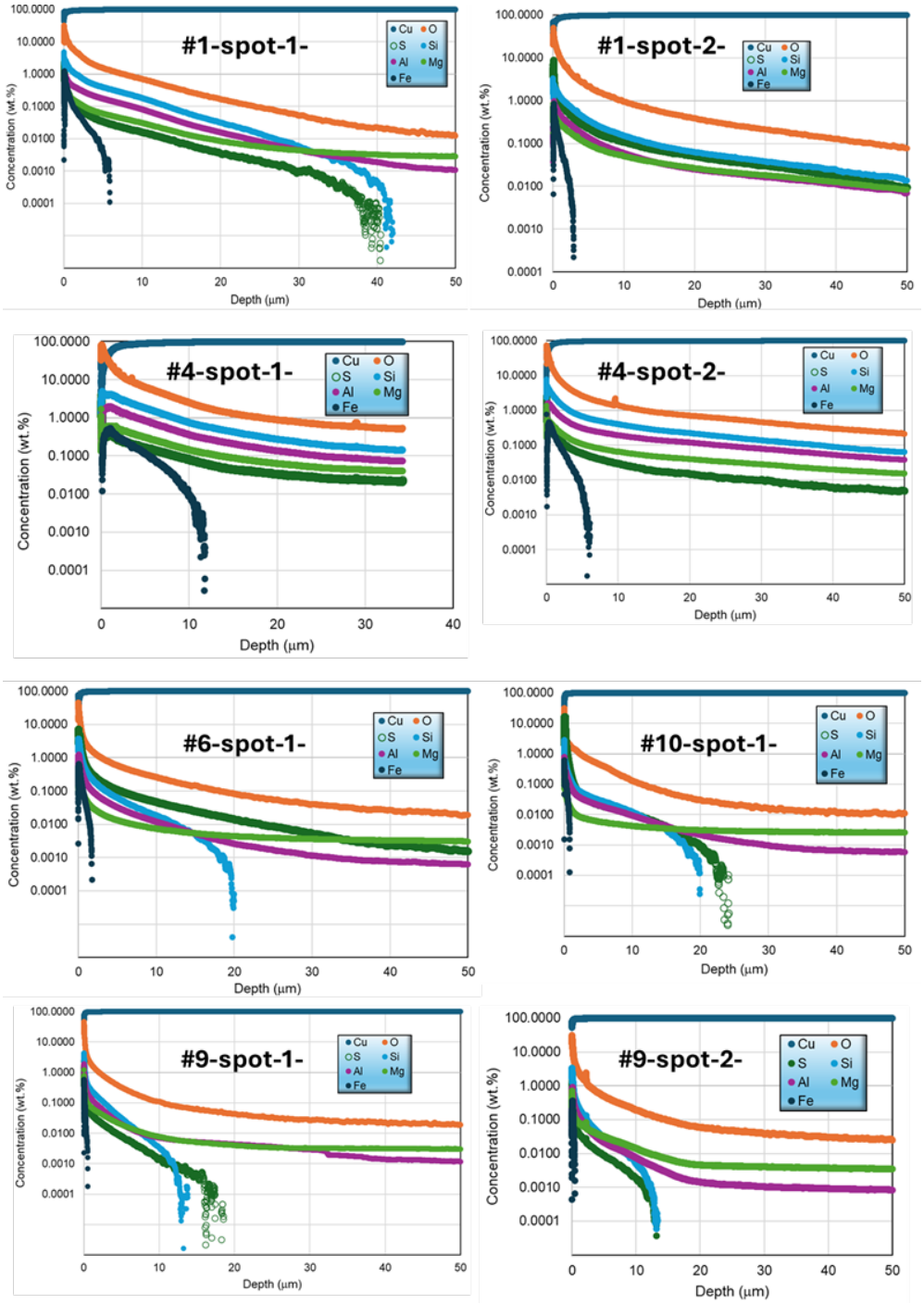

Figure 15. *Elemental depth profile obtained by GDOES on the surface of the exposed copper samples from canister.*

3.3.3 XRD

XRD analysis was performed on six exposed sample surfaces in their as-received state to identify corrosion products, as shown in Figures 16 to 21. In addition to metallic Cu, characteristic peaks of cuprite (Cu_2O) were observed on most detected samples. This is consistent with previous findings from field test (Wendel et al. 2022). Moreover, besides Cu and Cu_2O, gypsum ($Ca(SO_4)\cdot 2H_2O$) was identified on the white area of sample #1 (Krejsová 2024), and paratacamite ($Cu_2(OH)_3Cl$) on the green area of sample #4. Gypsum was mentioned to be one of the bentonite accessory minerals (Johanson et al. 2020).

There is also an indication of TiO_2 on sample #6 which was attributed to the white marker as confirmed by an SKB engineer. However, there was no substances other than Cu found by XRD from the surface of sample #8.

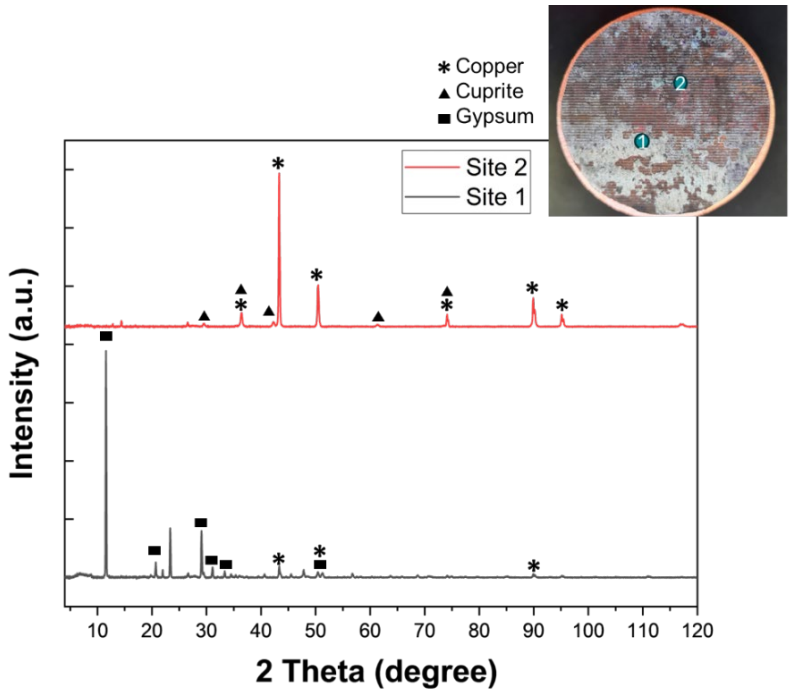

Figure 16. *XRD diffractograms obtained from the surface of sample #1. Inserted image shows the measurement locations.*

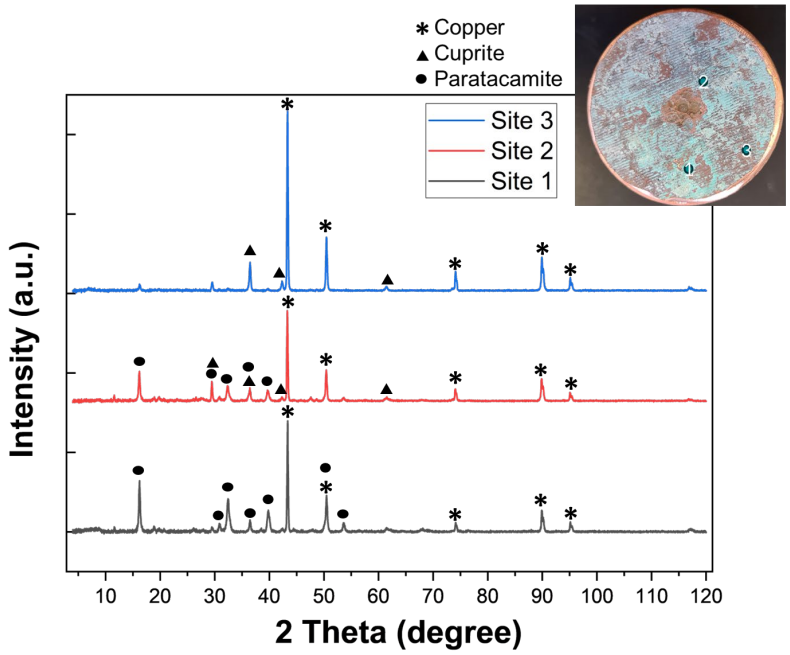

Figure 17. *XRD diffractograms obtained from the surface of sample #4. Inserted image shows the measurement locations.*

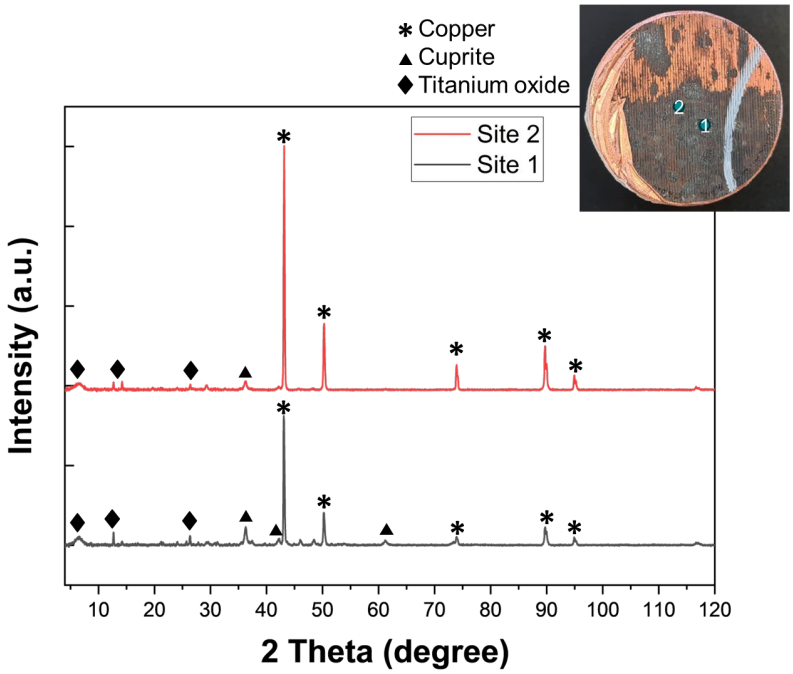

Figure 18. *XRD diffractograms obtained from the surface of sample #6. Inserted image shows the measurement locations.*

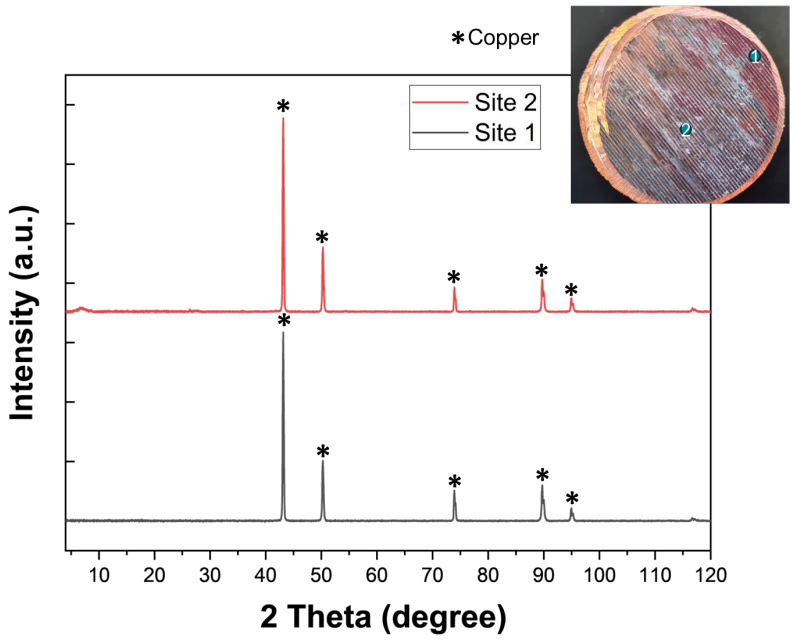

Figure 19. *XRD diffractograms obtained from the surface of sample #8. Inserted image shows the measurement locations.*

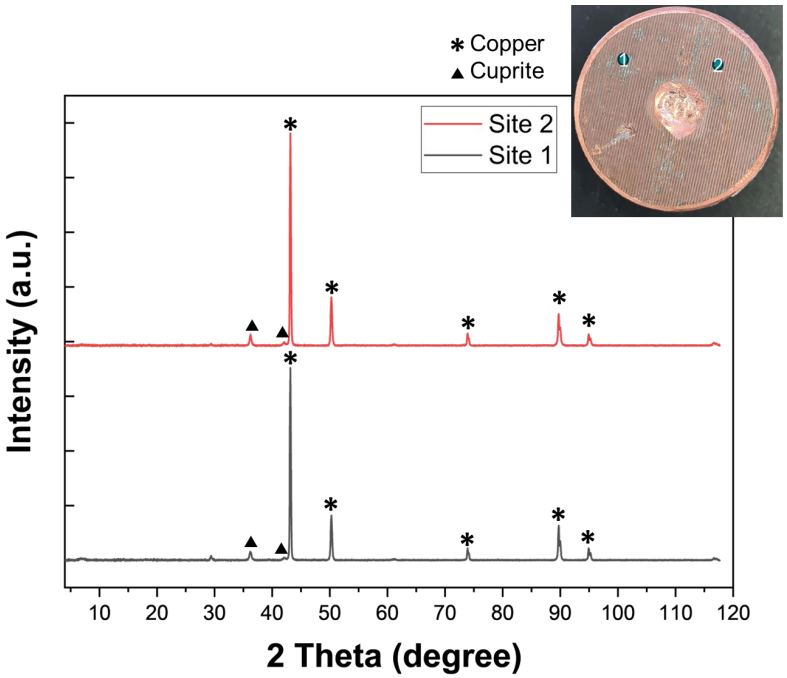

Figure 20. *XRD diffractograms obtained from the surface of sample #9. Inserted image shows the measurement locations.*

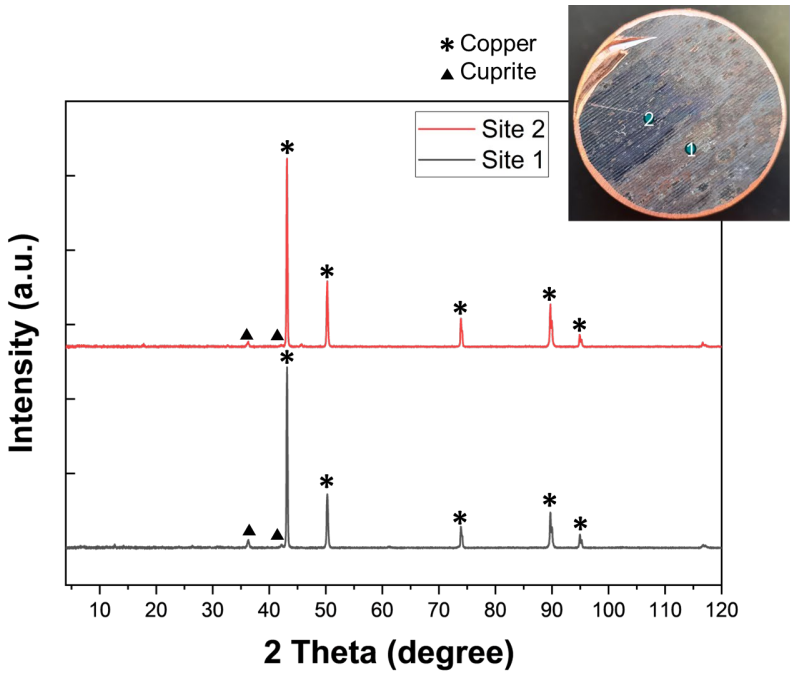

Figure 21. *XRD diffractograms obtained from the surface of sample #10. Inserted image shows the measurement locations.*

3.3.4 FTIR

To supplement XRD, the FTIR measurement can detect both crystalline and amorphous compounds locally. FTIR measurements were conducted on various sites defined according to their visually appearing colour on the six exposed samples. Figure 22 shows the FTIR analysis locations, and their corresponding spectra can be seen in Figures 23 to 28.

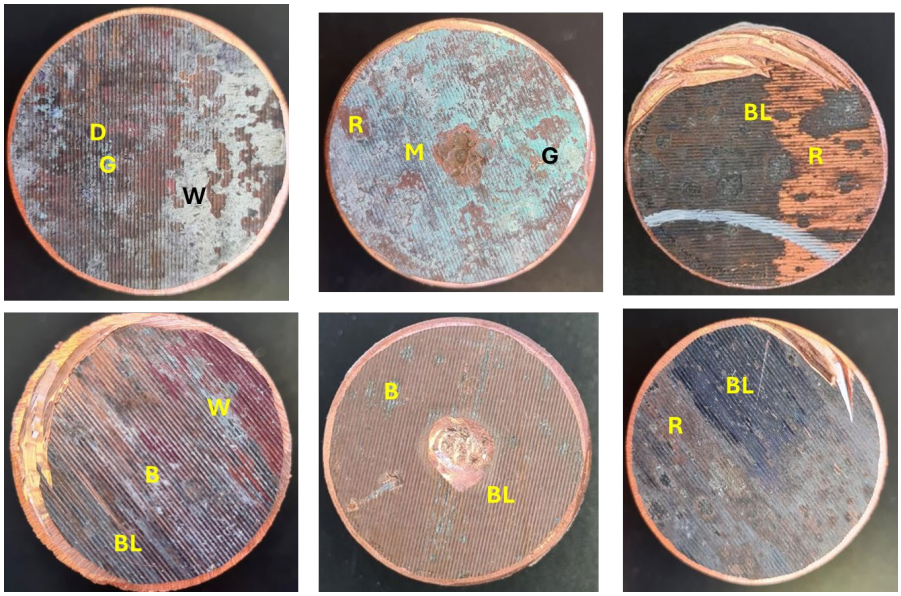

Figure 22. *Locations of FTIR analysis on the surface of samples. BL: black, B: bulk, D: dark, G: green, M: mixed, R: red, W: white.*

The characteristic cuprite (Cu_2O) absorbance band around 600 cm^{-1} in all measured areas confirmed the presence of this oxide corrosion product. In addition, two bentonite absorbance bands were identified at 1000 cm^{-1} and 3600 cm^{-1} for all samples (Kaur et al. 2021). Bands at 3300 cm^{-1} and 600 cm^{-1} for the samples #4, #6, and #10 are attributed to the presence of paratacamite ($OH(Cu_3(OH)_6Cl_2)$) (Welch et al. 2014). The spectra also indicated the existence of certain carbonates (CO_3^{2-}) present on the surface of all samples which may correspond to calcite as one of the bentonite mineral constituents. The areas measured from sample #8 and #9 exhibited −CH at around 2900 cm^{-1} which may correspond to some organic compound. Finally, a small peak at 1100 cm^{-1} was present in all samples and is suspected to correspond to sulphate group. Sulphate presence can be related to both groundwater and bentonite. The peaks at around 2340 cm^{-1} indicated gaseous CO_2, probably just related to the background CO_2 in the spectrometer.

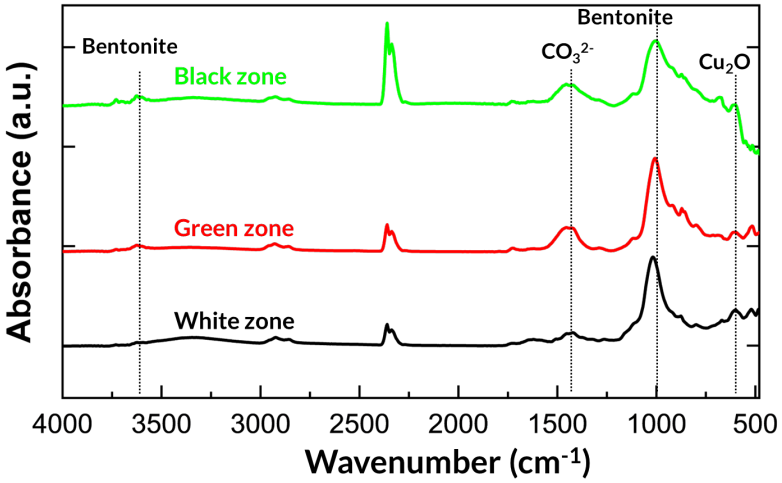

Figure 23. *Infrared spectra from FTIR measurement on the surface of sample #1.*

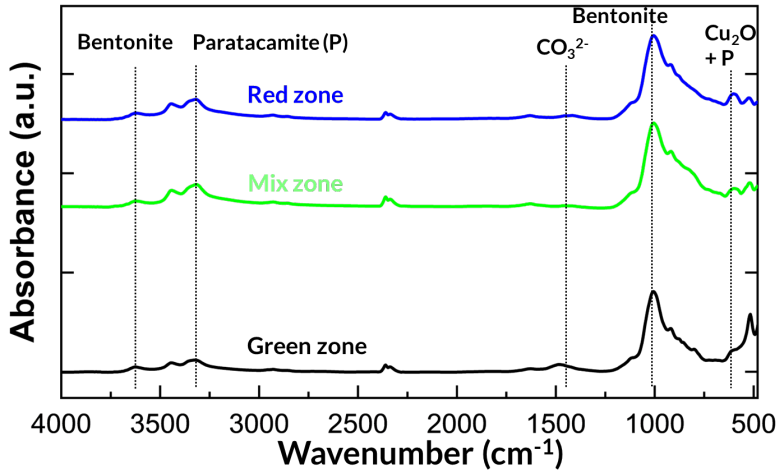

Figure 24. *Infrared spectra from FTIR measurement on the surface of sample #4.*

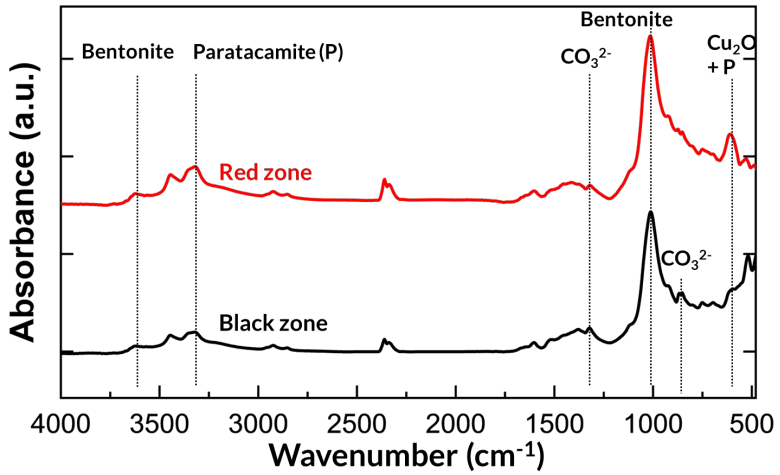

Figure 25. *Infrared spectra from FTIR measurement on the surface of sample #6.*

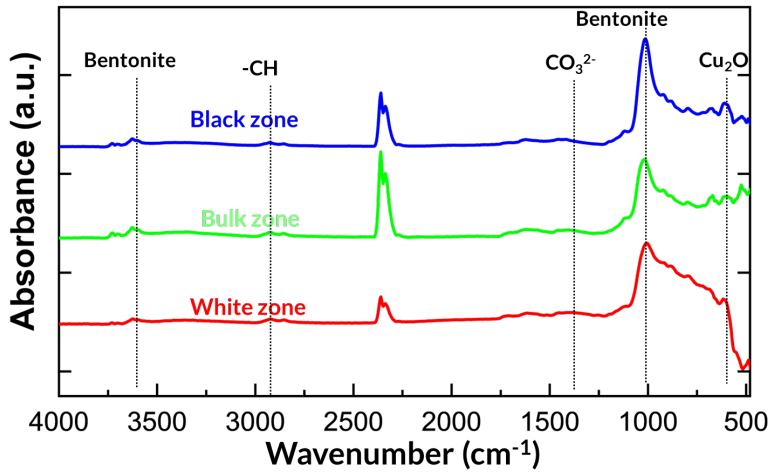

Figure 26. *Infrared spectra from FTIR measurement on the surface of sample #8.*

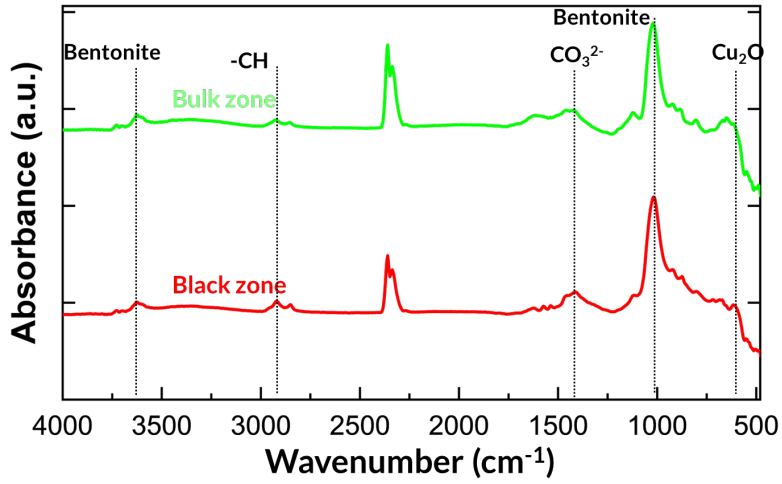

Figure 27. *Infrared spectra from FTIR measurement on the surface of sample #9.*

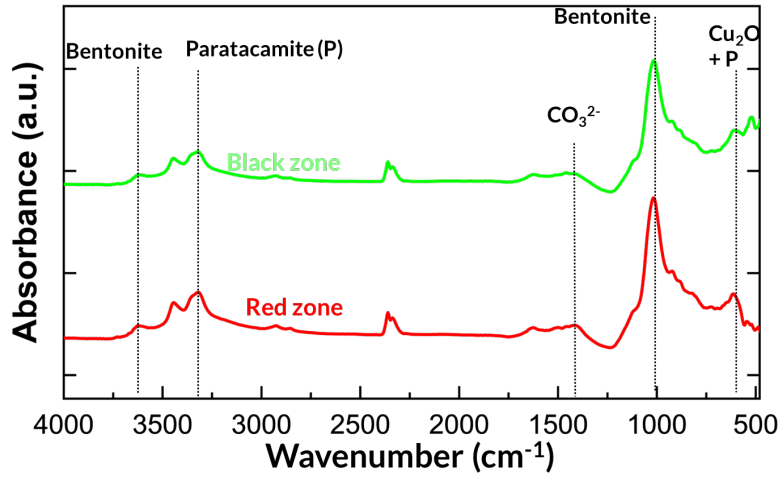

Figure 28. *Infrared spectra from FTIR measurement on the surface of sample #10.*

3.3.5 Raman

µ-Raman spectroscopy was also conducted on sample #10 since it showed a high amount of sulphur element through EDS analysis (Table 5), to explore further the possibility of sulphur-based corrosion products (CuS or Cu_2S) that could not be detected by XRD and FTIR. Typical Raman characteristic peaks of CuS or Cu_2S are expected to appear at 474 cm^{-1} (Chaki et al. 2014, Patil et al. 2018).

Eight different sites from the surface of sample #10 were analysed. Raman spectra of four representative different areas, along with the identified compounds are shown in Figure 29. The remaining area results can be found in Appendix B (Figure B-1). Most areas showed the presence of dehydrated copper chloride ($CuCl_2 \cdot 2H_2O$) (Medeiros et al. 2018) and montmorillonite clay (one of the bentonite constituents) characteristic Raman bands. The spectrum range beyond 1000 cm^{-1} (where further Raman bands of $CuCl_2.2H_2O$ exist) was not explored due to the purpose of this characterization (detection of sulfur-based corrosion products). In two other areas (6 and 8), with greenish appearance, the surfaces were detected with copper oxides (CuO, Cu_2O) and with dehydrated copper compound (Guha 1991, Debbichi 2012). Thus, Raman results confirmed previous XRD and FTIR findings.

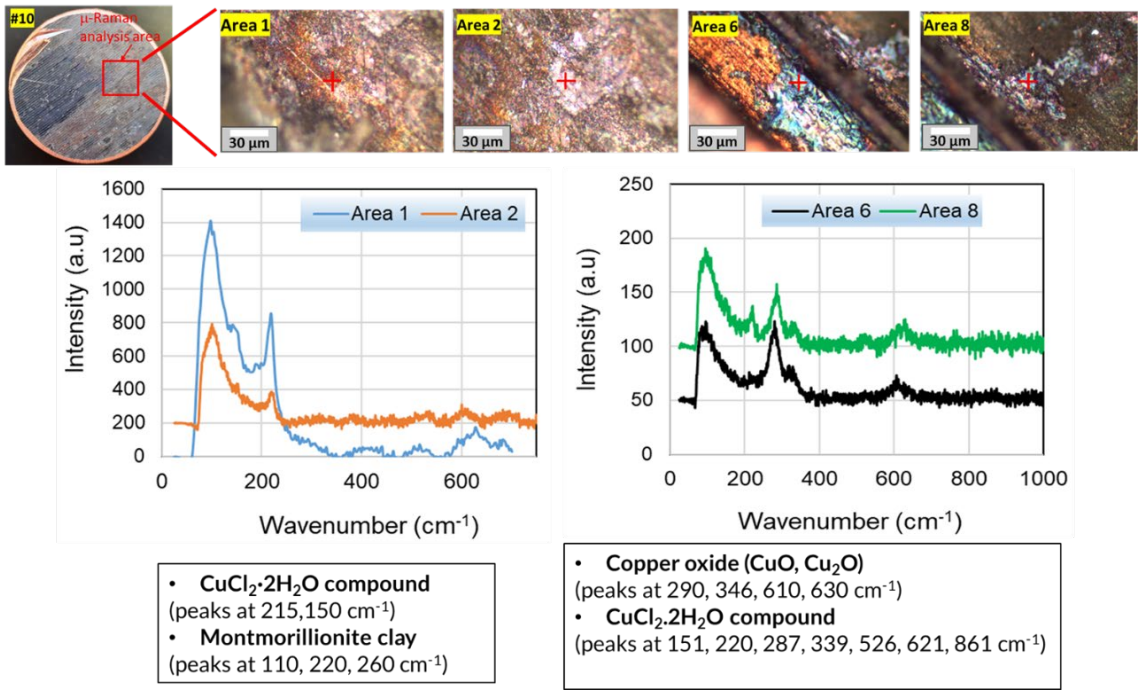

Figure 29. *µ-Raman measurement on different areas of the sample #10, and corresponding spectra and identified compound of four representative areas. The Raman spectra of other areas can be found in Appendix B.*

The different compounds detected by the three characterization techniques are summarized in Table 6. The obtained results agree with previous assessment findings (Taxén et al. 2012, Johansson et al. 2020).

Table 6. Summary of identified compound by XRD, FTIR, and µ-Raman

Sample	XRD	FTIR	µ-Raman
1	Cu_2O $Ca(SO_4)2H_2O$	Bentonite Cu_2O CO_3^{-2} SO_4^{-2} (?)	N/A
4	$Cu_2(OH)_3Cl$ Cu_2O	Bentonite $OH(Cu_3(OH)_6Cl_2)$ Cu_2O CO_3^{-2} SO_4^{2-} (?)	N/A
6	Cu_2O TiO_2	Bentonite $OH(Cu_3(OH)_6Cl_2)$ Cu_2O CO_3^{-2} SO_4^{2-} (?)	N/A
8	Nothing except Cu	Bentonite CO_3^{-2} Cu_2O −CH SO_4^{2-} (?)	N/A
9	Cu_2O	Bentonite CO_3^{-2} Cu_2O −CH SO_4^{2-} (?)	N/A
10	Cu_2O	Bentonite CO_3^{-2} $OH(Cu_3(OH)_6Cl_2)$ Cu_2O SO_4^{2-} (?)	Dihydrated copper compound (e.g., $CuCl_2{\cdot}2H_2O$) Montmorillonite clay[8] Copper oxides (CuO, Cu_2O)

N/A – Not analysed

[8] A typical bentonite constituent

3.4 Cross-section analysis

3.4.1 SEM-EDS

The aim of this part is to complete the chemical information on the surface products in cross-sectional orientation, explore the possibility of localized attack and its extent and surrounding chemistry, and discuss the surface layer in terms of adhesion, porosity and so on. Due to the absence of surface product layer, sample #9 was excluded from this part of analysis. Locations of cross-section samples is shown in Appendix C-Fig. C-1).

Figure 30 shows cross-section SEM images on sample 1 with a quite continuous layer with different thickness and with some cracks. That layer was identified to be bentonite based on its typical major chemical elements such as Ca, Mg, Si, and Al (Table 7). No significant underneath corrosion attack could be observed. Some sulphur was detected on both location 1 (bentonite) and between the pure copper and bentonite layer. It is not obvious to attribute it to a local corrosion process when considering that sulfur can be attributed to the present gypsum identified on this sample surface by XRD (Figure 16). Such compound can be related to the groundwater and/or bentonite as discussed in previous studies (King et al. 2010, Johannsson et al. 2020).

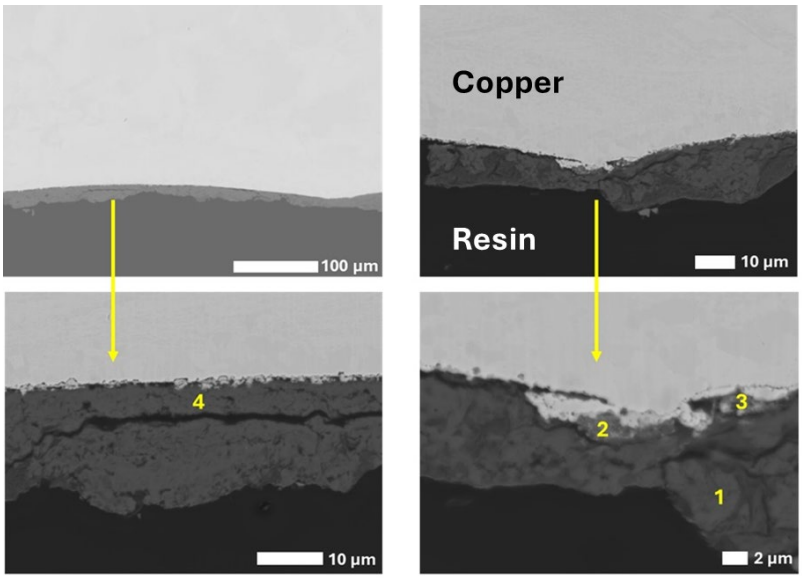

Figure 30. *SEM images of cross-section on sample 1.*

The detection of some chlorides on sample 4 cross-section is consistent with both XRD and FTIR findings with paratacamite compound. Sample 6 showed a porous and thin (~3 µm) corrosion layer that contains significant amount of sulphur and little oxygen. This very thin layer is challenging to determine its specific compound by the conventional characterization techniques that were used in the present assessment. The presence of chloride and oxygen on cross-section of sample 8 may indicate the possibility of oxychloride copper product which was not detected by XRD or FTIR. The presence of local sulphur combined with oxygen on cross-section of sample 10 would support more the presence of sulphates as highlighted in FTIR result (Figure 28) despite the presence of porous corrosion layer with limited extent. Additional SEM images at lower magnification are gathered in Appendix D.

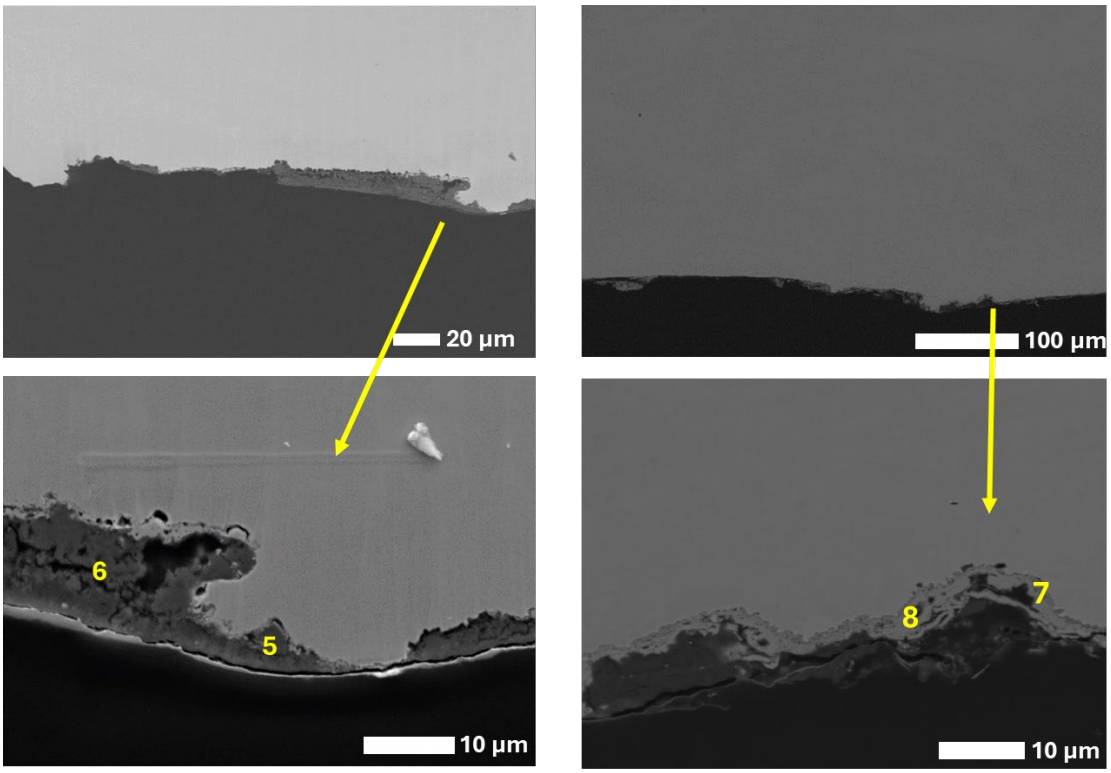

Figure 31. *SEM images of cross-section on samples 4 (left) and 6 (right).*

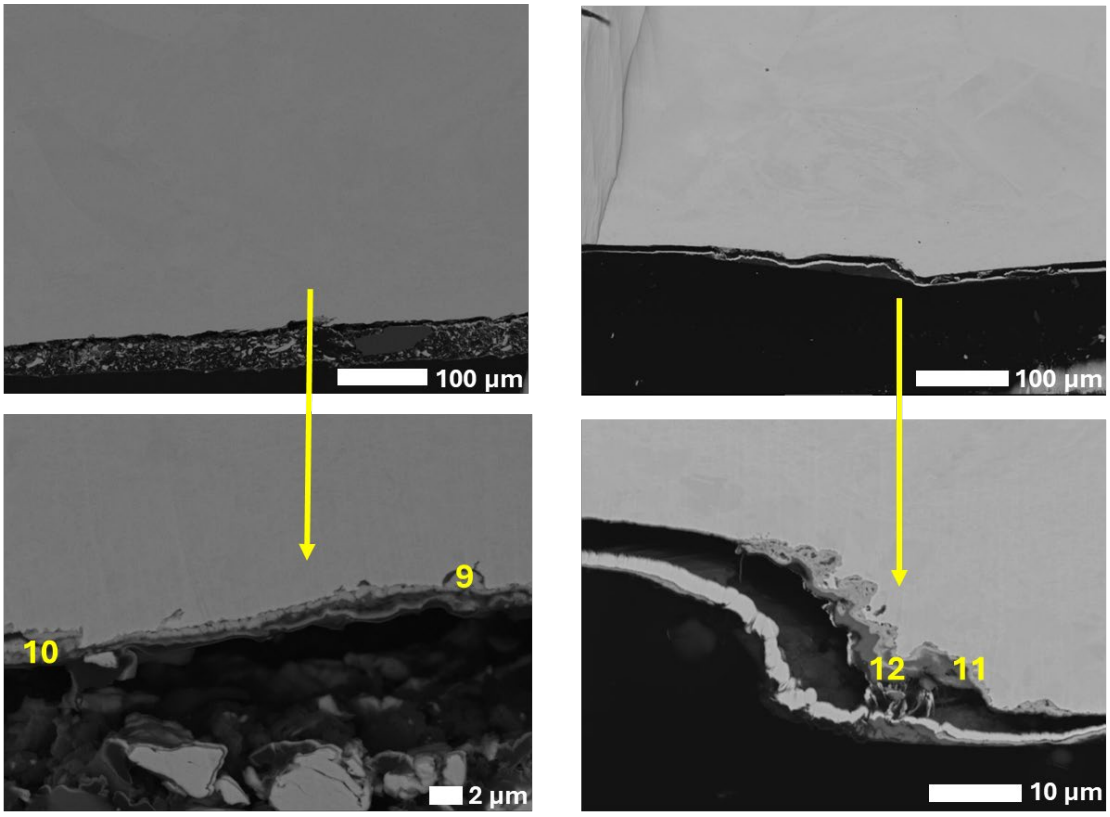

Figure 32. *SEM images of cross-section on samples 8 (left) and 10 (right).*

Table 7. EDS analysis on cross-section for the different studied samples

Sample	Site	Element (at. %)								
		Cu	O	Cl	S	Mg	Al	Si	Ca	Fe
1	1	1.4	52.1	-	1.1	1.8	1.9	5.9	35.3	0.4
	2	24.2	37.8	0.7	2	2.3	1.4	5.1	25.5	0.9
	3	90.6	6.8	-	-	-	-	1.1	-	-
	4	74.9	18.2	2.2	-	-	-	1	3.7	-
4	5	59.3	21.7	1.3	0.3	1.3	-	0.2	15.9	-
	6	5	51.5	0.8	0.9	3.3	0.8	3.6	34.6	-
6	7	68.3	9.4	-	22.1	-	-	-	-	-
	8	67.8	8	-	24.1	-	-	-	-	-
8	9	70.5	25.9	2.9	0.4	-	-	0.04	-	-
	10	74.4	20.2	1.5	0.17	-	-	0.04	-	-
10	11	60.2	33.6	-	2.8	1.7	-	-	1.5	-
	12	70.5	13.6	0.8	15.1	-	-	-	-	-

3.4.2 Electron Backscatter diffraction (EBSD)

EBSD allows to determine the local crystal structure and crystal orientation at the surface of a metal. Figure 33 shows the EBSD analysis for five samples and sample 9 was excluded due to the absence of corrosion or surface product layer. Crystalline orientation for the different samples seems variable. However, it is not possible to draw any conclusion on the statistics of grain size or orientation due to the small, analysed surface area and big and variable grain size. Also, some plastic deformation within grains could be noticed at the grain boundaries. For some samples such as samples 1 and 10, this is seen in the IPFZ (Inverse Pole Figure in Z direction) in Figure 33. For all samples, this can be seen in the average missorientation maps, in Appendix E -Figure E-1.

Further, indication of plastic deformation zone (appearing as black zone) was noticed for all samples associated with grain refinement at the surface in contact with bentonite clay. The grain refined zone may include corrosion product which could not be distinguished by EBSD. This can be due to the corrosion layer which is thinner (than grain refined zone) and not continuous as revealed by SEM-EDS on cross-section samples. The plastic deformation associated with grain refinement may have two possible explanations i.e. the surface machining process that the copper canister surface has been subjected to or samples preparation prior to EBSD analysis. The last possibility was excluded for two reasons i.e. the absence of this plastic deformation when moving to the bulk material and considering that the BIB treatment can remove up to 60 μm in depth which may exclude a great part of cutting artefacts.

On the other hand, literature survey shows that surface machining was found to induce grain deformation, recrystallization and refinement due to the temperature increase associated with stress (Pan et al. 2017). The recrystallization temperature of oxygen free pure copper reported in literature is ranged between 379.05 °C to 433.2 °C (Su et al. 2021). The consequence of this microstructure alteration consists in the improvement of the corrosion resistance with less tendency for pitting corrosion (Lapeire et al. 2017). Also, the mechanical yield strength was found to improve with grain refinement without losing fracture elongation (Zhang et al. 2020). In this case, the very low corrosion extent can be related to this microstructural aspect. Further investigation on this hypothesis should be undertaken.

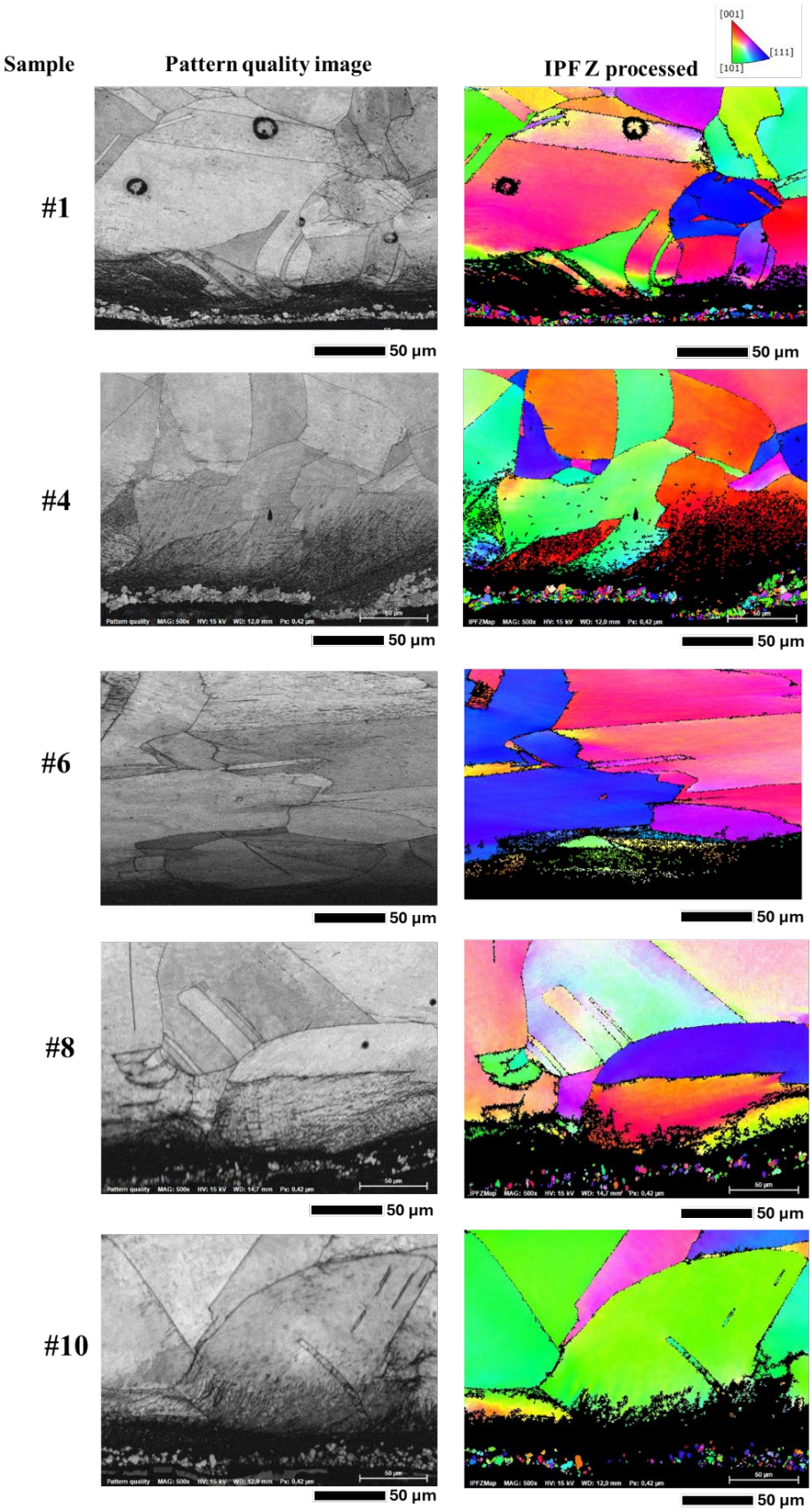

Figure 33. *EBSD analysis on cross-section samples. Pattern quality map (left), processed IPF[9] Z (right).*

[9] Inverse pole figure

3.5 Corrosion attack

3.5.1 Surface topography

The surface topography before and after chemical pickling is shown in Figure F-1 (Appendix F). The surface topography of the samples was examined using optical profilometer both before and after the removal of corrosion products by pickling, as shown in Figures 34. Mechanically damaged zones are excluded when applicable. Surface profile measurements showed clearly that the surface striations are attributed to the machining of the canister. Their measured height is equal to 10 μm and is relatively sharp, see the line profiles of each sample in the Appendix F, Figure F-2. The height of striations determined by the optical profilometer on non-pickled samples was found between 12 and 17 μm in previous characterization (Taxén et al. 2012). Through these line profiles, corresponding to the topographic analysis before pickling, it can be found that the maximum surface product height reaches 50 μm. This height includes the contribution of existing surface products such as bentonite, gypsum, and corrosion oxide products.

The sample surface roughness (estimated using ISO 25187 procedure) comparison of the maximum height (S_z) and the average height (S_a) before and after pickling can be found in Figure 35. Notice that each pickled sample surface area represents 50 % of the total original sample area approximately. It is observed that the maximum height on the surface relative to the mean plane is lower for the pickled samples, which confirms the removal of corrosion/surface products for all samples. However, the average surface roughness before and after pickling is nearly the same, indicating that the surface features from machining dominates the surface roughness calculation thus makes the distinction of surface roughness due to corrosion and any possible metal substrate localized attack due to pickling quite uncertain. This was observed in previous studies (Högberg et al. 2017).

Sample 4 was selected to carry out a trial on one representative area of 25 mm^2 with analysis of surface defects and/or measurements of pit depths utilising different magnifications. The reason behind is related to the significant chloride amount detected on the surface of this sample, which could lead to possible pitting corrosion prior to the anoxic stage of the process where still some oxygen exists. Three different magnification objective lenses (5x, 20x, and 50x) with different resolutions (vertical and lateral) were considered to map the samples, as shown in Figure 36. Pitting analysis was performed using an advanced surface analysis software Mountains Map® wherein specific features that distinguish pits from general surface roughness (based on characteristics - such as depth, diameter, and shape) can be automatically detected and measured. The pitting analysis of a larger area (at 5x) did not yield good results as the pit depth determined was smaller than the resolution of the measurement. Higher magnifications (20x and 50x) gave more reliable results, but only smaller areas can be scanned. The pits under the surface products were quite small, between 2 and 6 μm deep (Table 8). This agrees with previous assessment (Taxén et al. 2012, Johansson et al. 2020) and cross-section samples examination (next section).

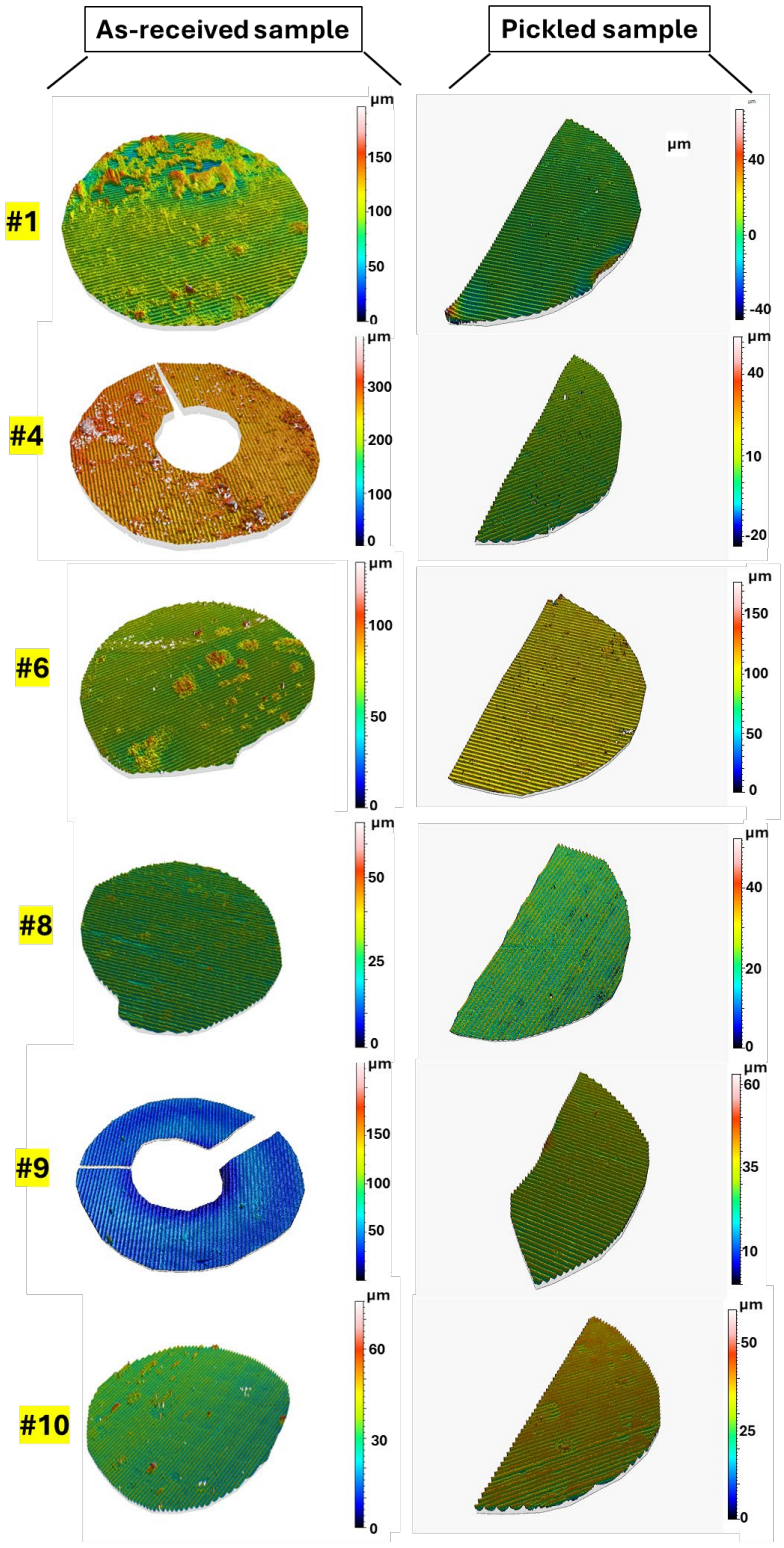

Figure 34. *3D surface topography of exposed samples before (left) and after (right) removal of corrosion products.*

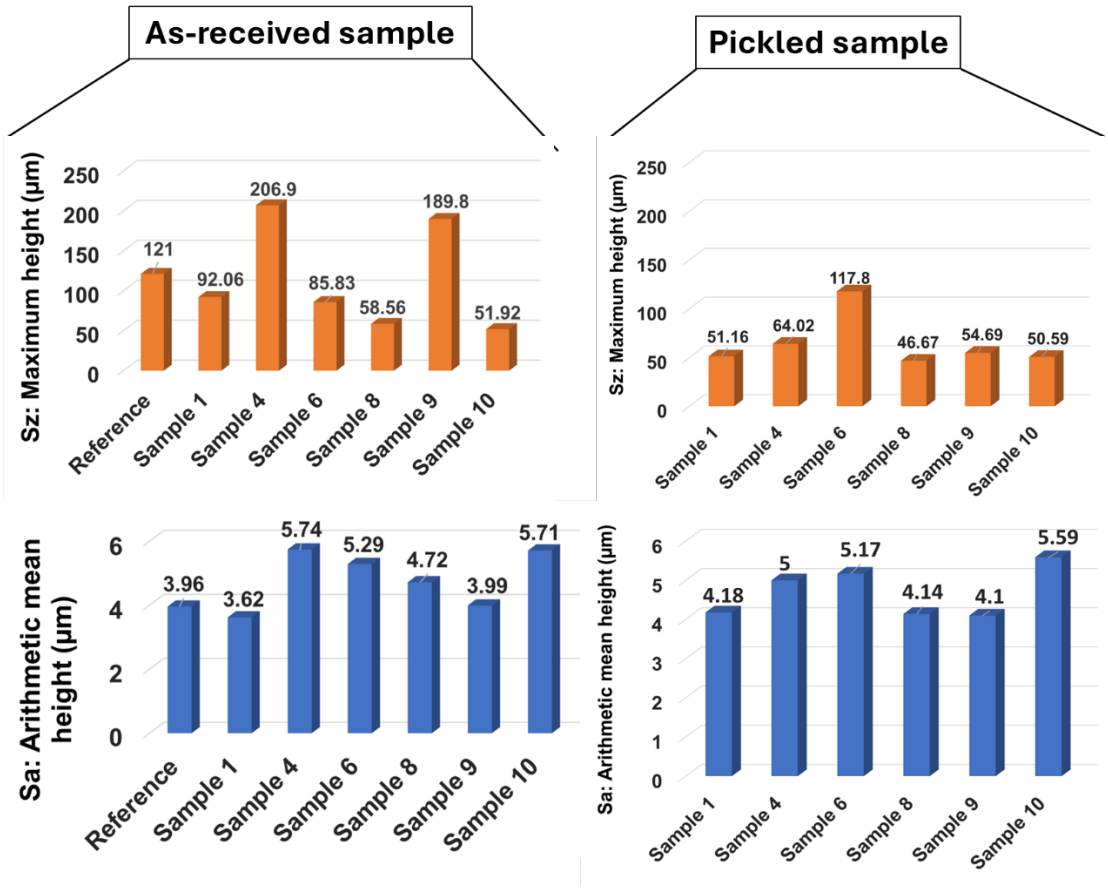

Figure 35. *Surface maximum height (µm) and mean height (µm) of samples before (left) and after (right) removal of corrosion products.*

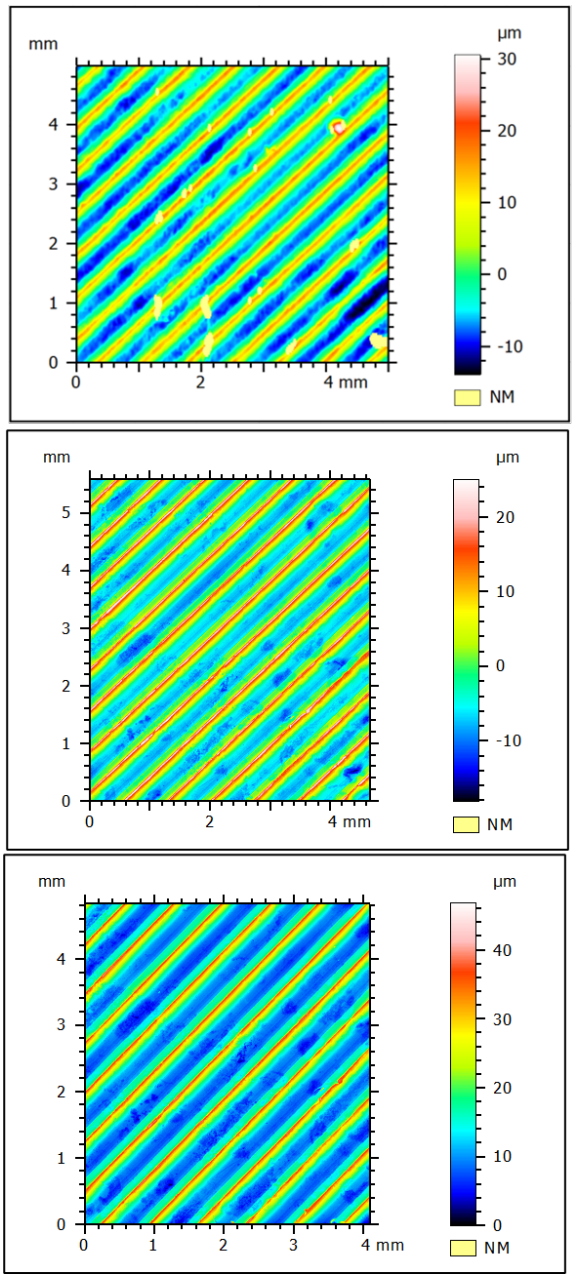

Figure 36. *Pit depth determination at different magnification of the sample #4 after removal of corrosion products.*

Table 8. Pit analysis on pickled sample 4.

5x		20x		50x	
Area (mm^2)	Pit depth (µm)	Area (mm^2)	Pit depth (µm)	Area (mm^2)	Pit depth (µm)
0.1232	3.1	0.0190	6.4	0.0119	5.4
0.0188	2.2	0.0019	3.5	0.0042	4.1
0.0058	0.8	0.0054	3.0	0.0014	4.0
0.0031	0.8	0.0025	2.6	0.0005	3.9
0.0000	0.6	0.0027	2.5	0.0052	3.7
0.0038	0.6	0.0001	2.3	0.0039	3.2
0.0001	0.5	0.0015	2.2	0.0039	3.1
0.0007	0.4	0.0002	2.1	0.0097	3.1
0.0003	0.3	0.0009	2.0	0.0026	3.0
0.0001	0.3	0.0039	2.0	0.0052	2.9

3.5.2 Cross-section examination.

Pit depths

The determination of pit depth through cross-section analysis under SEM showed some challenges. It was quite difficult to find typical pit forms since the copper corrosion attack was very limited and appearing more as surface roughness. Figure 37 shows example on samples 1 and 4 where attack depth did not exceed 3 to 5 µm. Moreover, in some cases the surface attack is close to certain observed porosity as seen for sample 4 in Figure 38.

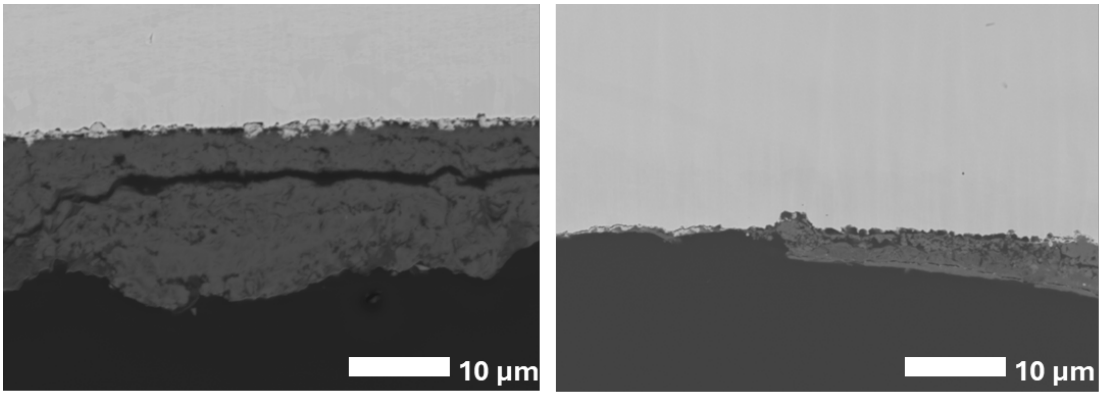

Figure 37. *SEM images showing surface corrosion attack on sample 1(left) and sample 4(right).*

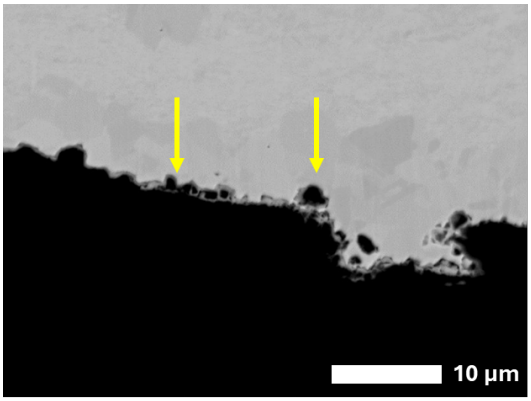

Figure 38. *SEM image of corrosion attack on sample 4.*

3.6 Hydrogen content measurement

Absorbed hydrogen quantification started on the reference copper sample taken from canister which had been stored indoor and was not exposed to the Äspö HRL conditions. Then, samples 10 and 8 were considered for investigation based on their sulphur amounts detected by EDS that suggest possible sulphur-based corrosion product that may develop under anaerobic corrosive conditions and would induce a possible hydrogen absorption. In total, 28 samples (9 from reference, 9 from sample #8, 10 from sample #10) were obtained for the various location in the sample to be analysed by HME or TDS. The hydrogen content analysis by HME of the samples was conducted at five to eight different depths into the metal including the top corroded surface and shown in Table 9. The results indicate through both methods that reference copper sample contains slightly more hydrogen than the exposed sample 10. This would exclude or reduce significantly the possibility of hydrogen pick up due to corrosion for sample 10. Moreover, the obtained range for the reference sample support that it originates from manufacturing process as reported in literature (Rajainmaki et al. 1993, Martinsson et al. 2013). However, sample 8 showed an average hydrogen content of 2.31 ppm measured by HME while the result from TDS remained in the same range as sample 10 and copper reference sample (~0.4 ppm).

The same range of 2 ppm was obtained in previous assessment (Granfors 2017, Johanson et al. 2020) and correlated to the corrosion product and surface deposit influences. Hydrogen profile by TDS technique was not explored in the present project due to the limitation of samples and limited present surface deposit amount. TDS curves are provided in Figures G-1 and G-2 (annex G) for samples 8 and 10 respectively.

It is known that TDS conditions (heating temperature) are different from HME which explain partially the deviation/difference in the results between these two techniques. For HME obtained values of sample 8, it is difficult to ascertain the source when compared to the sample 10 results. Two main possibilities may be highlighted in the light of the remaining results i.e. manufacturing defect (excessive microporosity in some locations -uneven porosity distribution-) or heterogenous distribution of absorbed hydrogen throughout the canister material.

Table 9. Hydrogen analysis by TDS and HME for Cu-reference sample, samples #8 and #10

Method	Sample	ID	Weight (g)	Volume (cm^3)	H (ppm)	Average H (ppm)
HME	Cu-Reference	2	0.853	0.125	0.62	0.38 ± 0.13
		3	0.932		0.36	
		4	1.026		0.36	
		5	0.870		0.34	
		6	0.859		0.26	
	Sample#8	2	1.118		2.35	2.31 ± 0.66
		3	1.150		2.57	
		4	1.104		1.90	
		5	1.200		2.05	
		6	0.949		3.56	
		7	0.901		2.64	
		8	0.997		2.13	
		9	1.389		1.28	
	Sample#10	3	0.951		0.37	0.22 ± 0.09
		4	0.917		0.22	
		5	0.794		0.20	
		6	1.101		0.19	
		7	0.927		0.20	
		8	1.026		0.10	
TDS	Cu-Reference	Left	16.763	29.926	0.47	0.41 ± 0.05
		Centre	20.286		0.45	
		Right	17.768		0.36	
		Behind	23.237		0.38	
	Sample#8		8.313		0.41	0.41
	Sample#10	Left	11.884		0.22	0.20 ± 0.03
		Centre	9.344		0.23	
		Right	10.407		0.20	
		Behind	24.285		0.15	

Figure 39 shows the hydrogen content profile obtained by HME from the corroded surface to the bulk material for the different tested samples where the first 5 mm samples include the corroded layer. As discussed above comparison of sample 10 with the reference gives that it is unlikely to have absorbed hydrogen because of corrosion. On the other hand, if it is assumed that for sample 8, the hydrogen source is a corrosion process, it can be expected that its hydrogen amount should decrease when moving from the corroded surface to the bulk material. However, this is not the case in the obtained result. Therefore, in such a case other factor may have affected the profile such as microstructure defects through which hydrogen could have diffused or progressed.

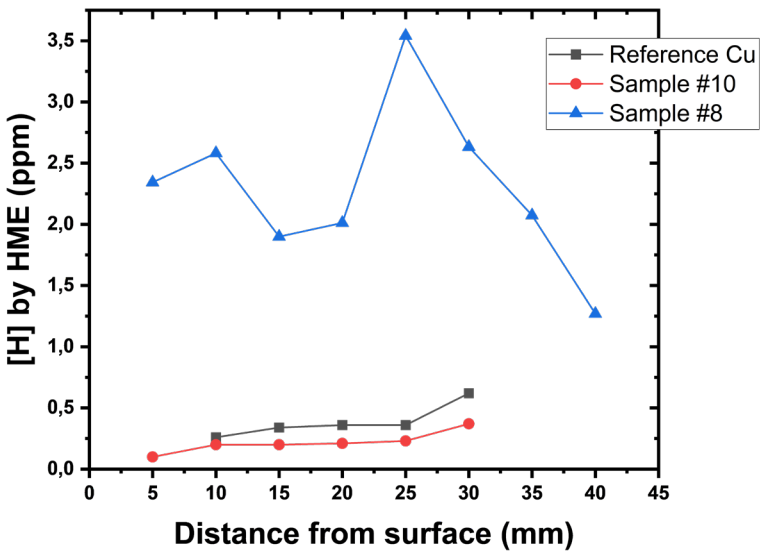

Figure 39. *Hydrogen content profile of reference and exposed copper samples as measured by HME technique.*

4 Discussions

The examination of obtained chemical information on the copper canister surface showed a variability in terms of compounds and their presence/distribution including bentonite, gypsum, copper oxide, and copper chloride product. From a corrosion perspective, copper oxide and copper chloride are typical compounds identified in previous assessment. Copper oxide seems present throughout the whole canister height while chloride-based corrosion product seems localized at the middle of the canister height (samples 4, 6 and 10).

For sulphur-based corrosion products, it was not possible to confirm their presence due to the limitations of the adopted techniques associated with the local character of the development of these corrosion products. From surface EDS elemental analysis, and excluding the sample 8 result, sulphur element distribution across the canister surface can be considered to decrease from the canister base to its top (Table 10). This trend is inversely proportional to the oxygen concentration. However, the oxygen content remains significant which would support more a sulphate group that can be related to the gypsum detected by XRD instead of sulphur-based copper corrosion product that would form under anoxic condition with some contribution from microorganisms (King et al. 2010). Such finding should be considered carefully when considering the local character of both limitations of the used techniques and the possible sulphur-based copper corrosion product.

Table 10. Vertical distribution of sulphur and oxygen elements concentration (maximum and average values) based on surface EDS analysis from Table 5

Sample	Distance from canister base (m)	Element concentration (at. %)			
		O max	S max	O av	S av
1	4.57	62.41	1.40	57.58	1.03
9	3.89	56.77	0.67	54.20	0.46
4	2.07	61.75	0.91	56.00	0.48
6	1.22	53.18	10.08	47.76	7.23
10	0.75	46.41	15.46	35.76	11.23
8	0.06	65.39	8.38	51.37	5.60

For the corrosion attack extent, despite some limitations in terms of technique and area representativity, both 3D optical surface profile and cross-section measurements showed very limited attack that do not exceed 3 to 6 μm respectively and which look like surface roughness more than typical corrosion pits. Similar attack level and morphology were also measured in previous field tests (e.g. outer section of prototype and LOT[10]), which indicate a low probability of localized corrosion especially if the surface chemistry results (corrosion products, bentonite, etc) are considered together with local micro-environment conditions (absence of oxygen, and $[Cl^-]/[CO_3^{-2}]$ ratio, buffering capacity of the bentonite). Previous studies excluded this risk mainly during the anoxic stage (King et al. 2013, King and Lilja 2014). However, Eriksson and Hermansson (1997) studied localized corrosion and passive layer possibility during the oxidizing period prior to the anoxic. Very little sign of passivity was observed by the authors through electrochemical measurements. In the same study, the authors claim a risk of pitting in absence of passive layer based on microscopic characterization in different conditions possible to develop in field. King and Lilja (2013) also checked this risk through the comparison between environmental conditions of canister and those reported in literature leading to copper pitting. The authors concluded that the risk is excluded, and the corrosion will be more general as surface roughening.

The present analysis brought another aspect related to the material microstructure near the outer surface exposed to the compact bentonite. Indication of plastic deformation associated with grain refinement was revealed by EBSD analysis, and it can be due to the canister surface machining. It is well established that grain refinement is favourable to higher corrosion resistance compared to non-machined surface. However, this aspect merits further investigation to conclude.

[10] Long Term Test of Buffer Material

In terms of hydrogen presence in the canister copper material, the two techniques used showed a similar level between the copper reference sample and sample 10, which selected based on its high sulphur content at the surface. This result supports manufacturing as a source of trapped hydrogen which is in line with the microporosity observed in the copper reference microstructure (Figure 8). Some deviation was noticed between TDS and HME for sample 8 which can be explained by the lower heating temperature in case of TDS that does not extract all possible hydrogen in the material. The slightly higher amount of hydrogen obtained by HME for this sample could not be determined in terms of source. Whereas the contribution of possible corrosion processes remains low, further analysis and more samples could help to clarify and determine its source.

5 Conclusions

Six copper samples were taken at different heights from a canister exposed to bentonite for 23 years. An extensive assessment was conducted on those samples combining different characterization techniques to determine the extent of corrosion, surface chemistry, microstructure features as well as possible hydrogen absorption.

The extent of localized corrosion remains very low and in agreement with previous assessments under similar conditions. A new finding from microstructure analysis through EBSD showed a possible impact of canister surface machining. Plastic deformation associated with grain refinement was observed near the exposed/corroded surface. The grain size decrease supports the improved localized corrosion resistance and may explain in part the very low extent of corrosion obtained in this assessment and maybe in other previous ones. This aspect merits further investigation under repository conditions.

The chemical composition of corrosion products and surface deposits showed variability including different compounds such as copper oxide (cuprite), copper hydroxychloride (paratacamite), bentonite and some inorganic scale (gypsum and carbonates). The possibility of sulphur-based corrosion product was not conclusive when combining all characterization results together. The corrosion layer observed in cross-section analysis was thin (less than ca 3 μm), discontinuous and had certain porosity. Finally, the amount of absorbed hydrogen measured for one sample (sample 10) by both HME and TDS remain below 0.4 ppm which is in accordance with previous assessments. The main source of this absorbed hydrogen appears to be from manufacturing process of the oxygen free pure copper. However, sample 8 showed slightly higher amount reaching 2 ppm but its source could not be ascertained where further analysis would be recommended.

References

SKB's (Svensk Kärnbränslehantering AB) publications can be found at www.skb.com/publications.

ASTM E407-07, 2015. Standard Practice for Microetching Metals and Alloys, ASTM International, United States.

Bodington J C, 2024 Casting high-conductivity oxygen free copper rod from scrap: myths and reality. UPCAST (upcast.com/green-perspective/)

Chaki S H, Tailor J P, Deshpande M P, 2014. Covellite CuS – Single crystal growth by chemical vapour transport (CVT) technique and characterization. Materials science in semi-conductor processing 27, 577-585.

Debbichi L, de Lucas M C M, Pierson J F, Krüger P, 2012. Vibrational Properties of CuO and Cu_4O_3 from First-Principles Calculations, and Raman and Infrared Spectroscopy. J. Phys. Chem. C 116, 10232−10237.

Eriksson S, Hermansson H P, 1997. Pitting corrosion of copper in nuclear waste disposal environments. Statens Kärnkraftinspektion Report 98:2.

Granfors M, **2017.** Round-robin of hydrogen content in copper determined by melt extraction and gas analysis. SKB R-17-15, Svensk Kärnbränslehantering AB.

Guha S, Peebles D, Terence Wieting T, 1991. Raman and infrared studies of cupric oxide. *Bull. Mater. Sci.* 14, 539–543.

Högberg C-J, Karlsson O, Randelius M, Johansson A J, 2017. Surface morphology and elemental composition of copper canisters for disposal of spent nuclear fuel. SKB P-17-11, Svensk Kärnbränslehantering AB.

Johansson A J, Svensson D, Gordon A, Pahverk H, Karlsson O, Brask J, Lundholm M, Malmström D, Gustavsson F, 2020. Corrosion of copper after 20 years exposure in the bentonite field tests LOT S2 and A3. SKB TR-20-14, Svensk Kärnbränslehantering AB.

Jönsson B, **Åkesson T, Jönsson B, Meehdi S, Janiak J, Wallenberg R, 2009.** Structure and forces in bentonite MX-80. SKB TR-09-06, Svensk Kärnbränslehantering AB.

Kaur H, Rana B, Tomar D, Kaur S, Jena K C, 2021. Fundamentals of ATR-FTIR Spectroscopy and Its Role for Probing In-Situ Molecular-Level Interactions. In: Singh, D.K., Pradhan, M., Materny, A. (eds) Modern Techniques of Spectroscopy. Progress in Optical Science and Photonics, vol 13. Springer, Singapore.

King F, Lilja C, 2013. Localised corrosion of copper canisters in bentonite pore water. SKB TR-13-27, Svensk Kärnbränslehantering AB.

King F, Lilja C, 2014. Localised corrosion of copper canisters. Corrosion Engineering, Science and Technology 49, 420–424.

King F, **Lilja C, Pedersen K, Pitkänen P, Vähänen M, 2010.** An update of the state-of-the-art report on the corrosion of copper under expected conditions in deep geologic repository. SKB TR-10-67, Svensk Kärnbränslehantering AB.

King F, Lilja C, Vähänen M, 2013. Progress in the understanding of the long-term corrosion behaviour of copper canisters. Journal of Nuclear Materials 438, 228–237.

Krejsová J, Kužel R, Keppert M, Scheinherrová L, Vimmrová A, 2024. New insight into the phase changes of gypsum. *Mater Struct* 57, 128.

Lapeire L, Lombardia E M, De Graeve I, Terryn H, Verbeken K, 2017. Influence of grain size on the electrochemical behavior of pure copper, J Mater Sci. 52, 1501–1510.

Martinsson Å, Sandström R, Lilja C, 2013. Hydrogen in oxygen-free, phosphorus doped copper: charging techniques, hydrogen contents and modelling of hydrogen diffusion and depth profile. SKB TR-13-09, Svensk Kärnbränslehantering AB.

Medeiros F E O, Araujo B S, Ayala A P, 2018. Raman spectroscopy investigation of the thermal stability of the multiferroic $CuCl_2$ and its hydrated form. Vibrational spectroscopy 99, 1-6.

Nagumo M, 2023. Hydrogen Trapping and Its Direct Detection. In: Fundamentals of Hydrogen Embrittlement. Springer, Singapore. https://doi.org/10.1007/978-981-99-0992-6_2

Olofson J, 2023. Hydrogeochemical groundwater monitoring. Results from water sampling in the Forsmark area 2022. SKB P-23-10, Svensk Kärnbränslehantering AB.

Pan Z, Feng Y, Liang S Y, 2017. Material microstructure affected machining: a review. Manufacturing Rev. 4, 5.

Patil S, Bagade C S, Joshi M P, Kharade S D, Khot K V, Mali S S, Hong C K, Bhosale P N, 2018. Facile hydrothermal assisted synthesis of time dependent Cu_2S thin films for efficient photoelectrochemical application. J Mater Sci: Mater Electron 29, 19322–19335

Rajainmaki H, Helenius A, Kolehmainen M, 1993. The Production and Application of Oxygen-Free Copper, Features forum March, 68-70.

SKB, 2010. Design, production and initial state of the canister. SKB TR-10-14, Svensk Kärnbränslehantering AB.

SKB, 2011. Long-term safety for the final repository for spent nuclear fuel at Forsmark. Main report of the SR-Site project. Volume 1. SKB TR-11-01, Svensk Kärnbränslehantering AB.

SKB, 2019. Supplementary information on canister integrity issues. SKB TR-19-15, Svensk Kärnbränslehantering AB.

SKB, 2022a. Post-closure safety for the final repository for spent nuclear fuel at Forsmark. Main report, PSAR version. SKB TR-21-01, Svensk Kärnbränslehantering AB.

SKB, 2022b. Post-closure safety for the final repository for spent nuclear fuel at Forsmark. Fuel and canister process report, PSAR version. SKB TR-21-02, Svensk Kärnbränslehantering AB.

Shindo D, Oikawa T, 2002. Energy Dispersive X-ray Spectroscopy. In: Analytical Electron Microscopy for Materials Science. Springer, 81-102.

Swedish Corrosion Institute and its reference group, 1978. Copper as a canister material for unreprocessed nuclear waste - evaluation with respect to corrosion. KBS TR 90, Svensk Kärnbränsleförsörjning AB.

Su Z, Zhu Z, Zhang Y, Zhang H, Xiao Q, 2021. Recrystallization behavior of pure Cu connection interface with ultrasonic welding. Metals 11, 61.

Sunny group, 2023. The difference between the performance of low-oxygen copper rod and oxygen-free copper rod, (https://www.sunymachine.com/NEWS/performance-of-low-oxygen-copper-rod-and-oxygen-free-copper-rod.html).

Taxén C, 2013. Ytprofiler på kopparkapslar från deponeringshål 5 och 6 i försöksserien Prototyp. SKB P-13-50, Svensk Kärnbränslehantering AB.

Taxén C, Lundholm M, Persson D, Jakobsson D, Sedlakova M, Randelius M, Karlsson O, Rydgren P, 2012. Analyser av koppar från prototypkapsel 5 och 6. SKB P-12-22, Svensk Kärnbränslehantering AB.

Tefera A G, Sinha D K, Gupta G, 2023. Experimental investigation and optimization of cutting parameters during dry cutting process of copper alloy. Journal of Engineering and Applied Science 70, 145.

Zhang R, Li Z, Sheng X, Gao Y, Lei Q, 2020. Grain refinement and mechanical properties improvements in a high strength Cu–Ni–Si alloy during multidirectional forging, Fusion Engineering and Design 159, 11176.

Wendel E, Gordon A, Börjesson E, Wärnheim A, Bergendal E, Johansson J, Svensson D, 2022. Analysis of corrosion products on filter housings in the Lasgit field experiment. SKB TR-22-01, Svensk Kärnbränslehantering AB.

Welch M D, Sciberras M J, Williams P A, Leverett P, Schlüter J, Malcherek T, 2014. A temperature-induced reversible transformation between paratacamite and herbertsmithite. Phys Chem Minerals **41**, 33–48.

Appendix A

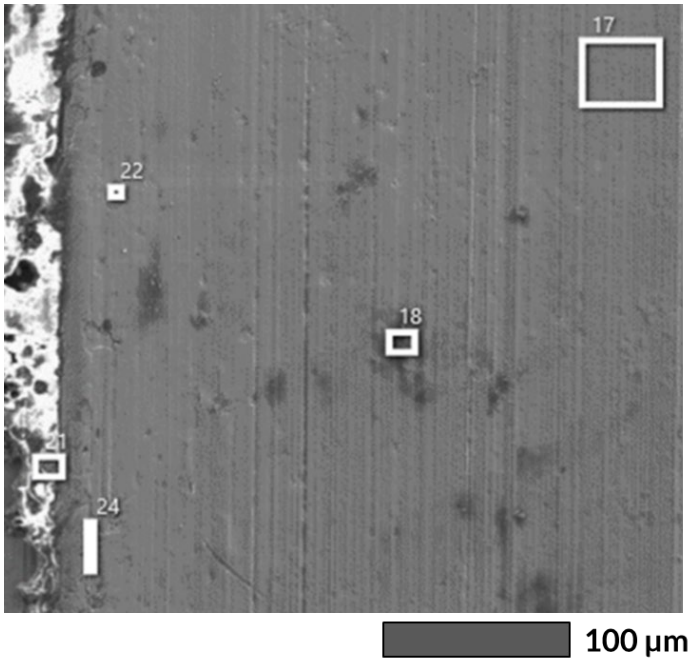

Location	Element (at. %)											
	O	Na	Mg	Al	Si	S	Cl	K	Ca	Fe	Cu	Mo
Spectrum 17	14.29	-	-	-	-	22.21	-	-	-	-	63.5	-
Spectrum 18	53.03	1.78	1.39	7.4	16.69	5.76	-	0.53		-	13.42	-
Spectrum 21	45.87	1.97	1.14	5.67	16.2	13.44	0.94	-	3.51	1.66	5.31	4.3
Spectrum 22	34.44	-	-	3.51	6.46	-	-	-	-	-	55.6	-
Spectrum 24	20.97		-	-	1.66	10.92	-	-	-	-	66.44	-

Figure A-1. *SEM image (up) and associated EDS analysis results (down) from sample #10 at site 2.*

Appendix B

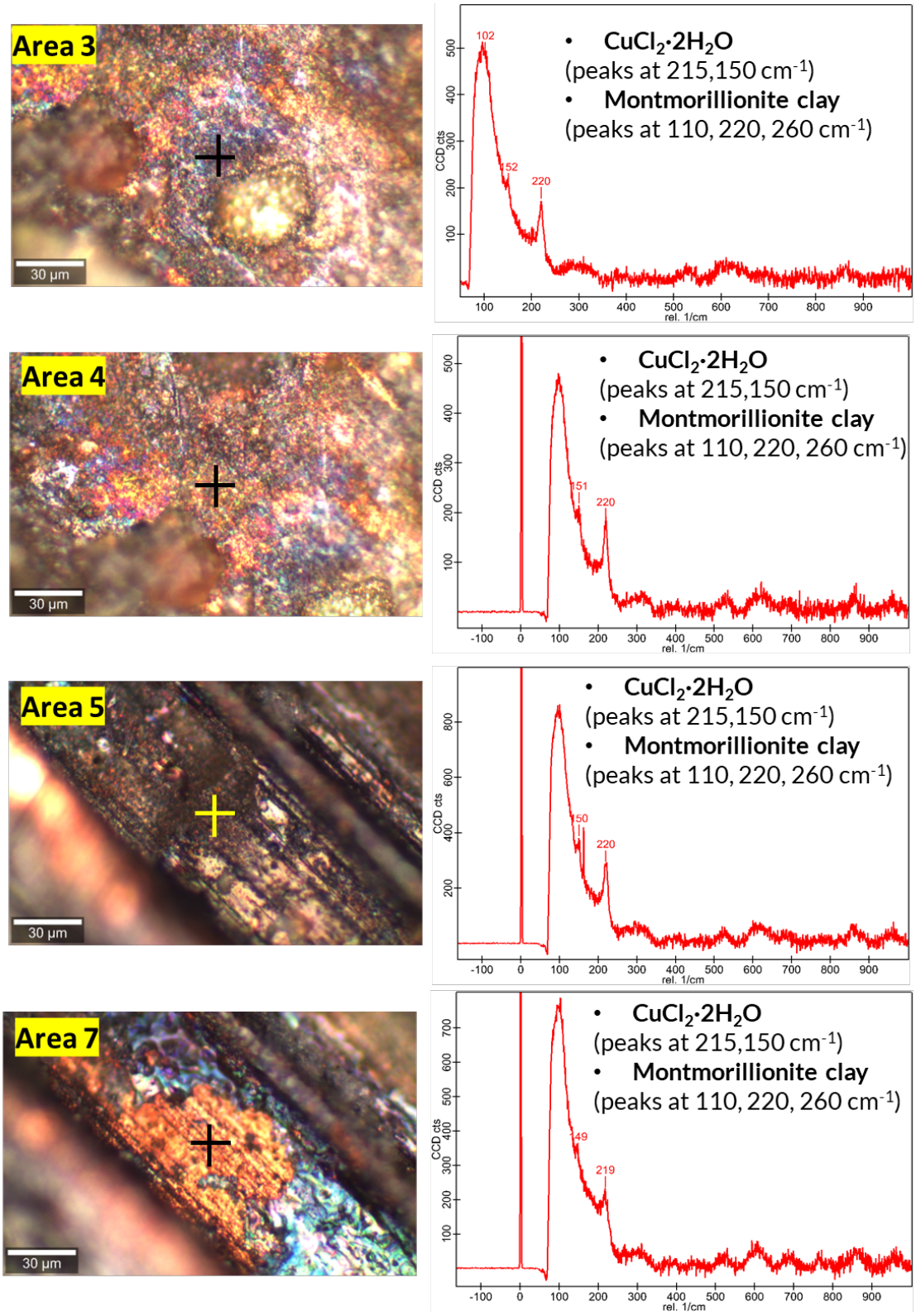

Figure B-1. *µ-Raman spectra on four different areas of the sample #10, and corresponding spectra and identified compounds (analysis location indicated by cross mark).*

Appendix C

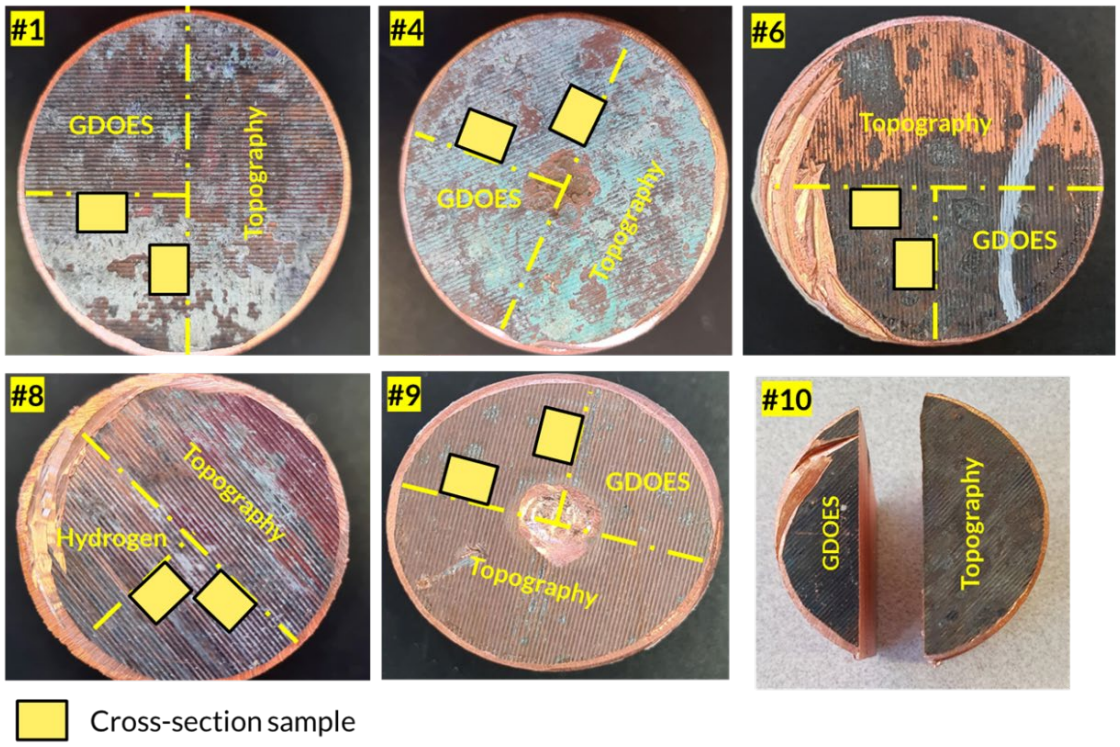

Figure C-1. *Locations of cross-section samples.*

Appendix D

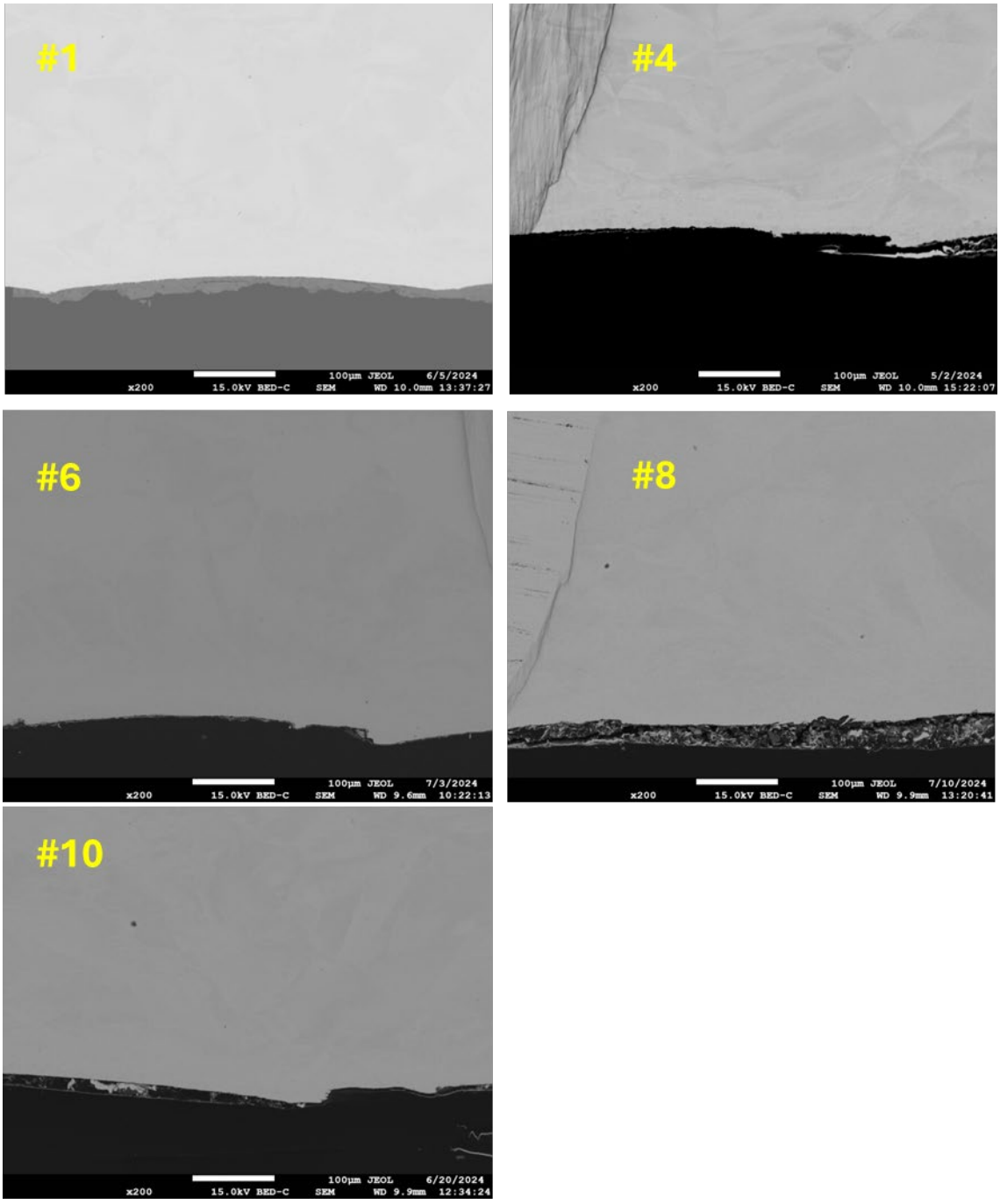

Figure D-1. *SEM images of pure copper cross-section samples at lower magnification (X200) in backscattered mode.*

Appendix E

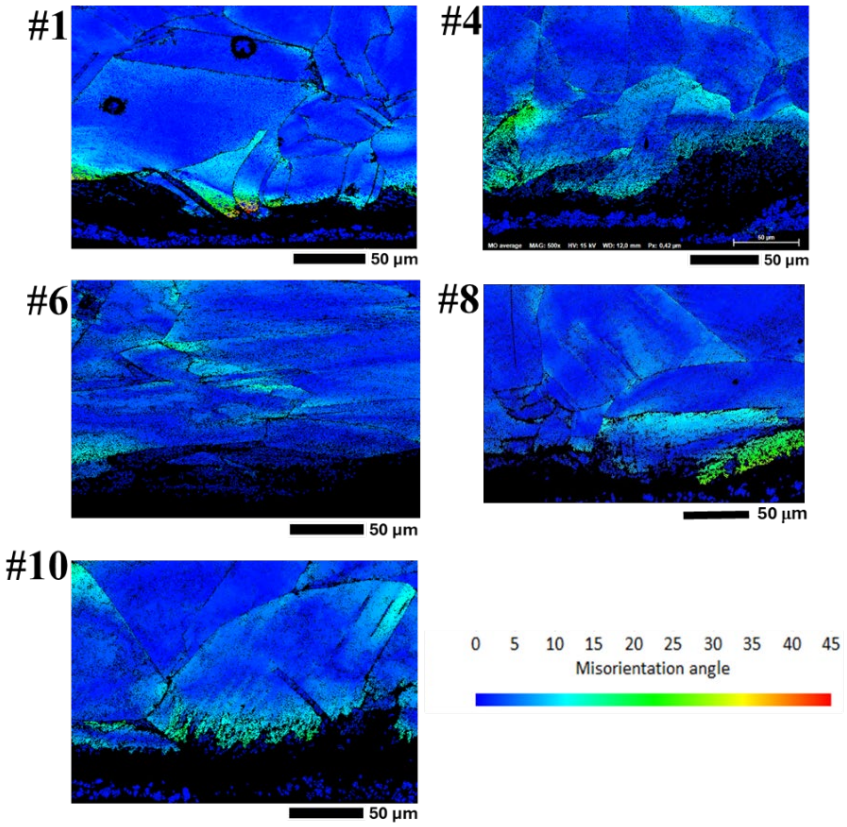

Figure E-1. *EBSD analysis of average misorientation angle on cross-section samples.*

Appendix F

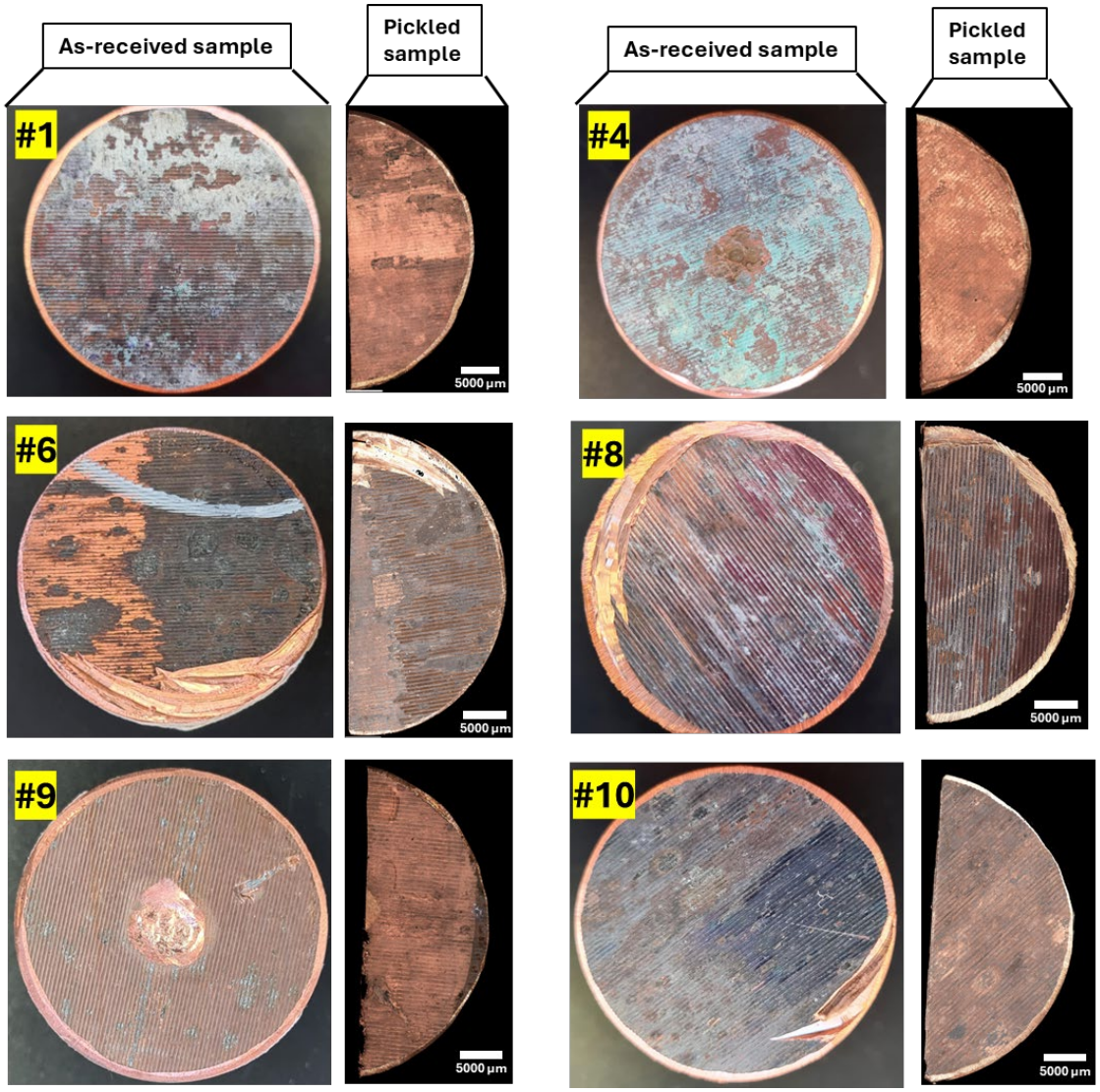

Figure F-1. *Images of exposed samples before (left) and after (right) removal of corrosion products.*

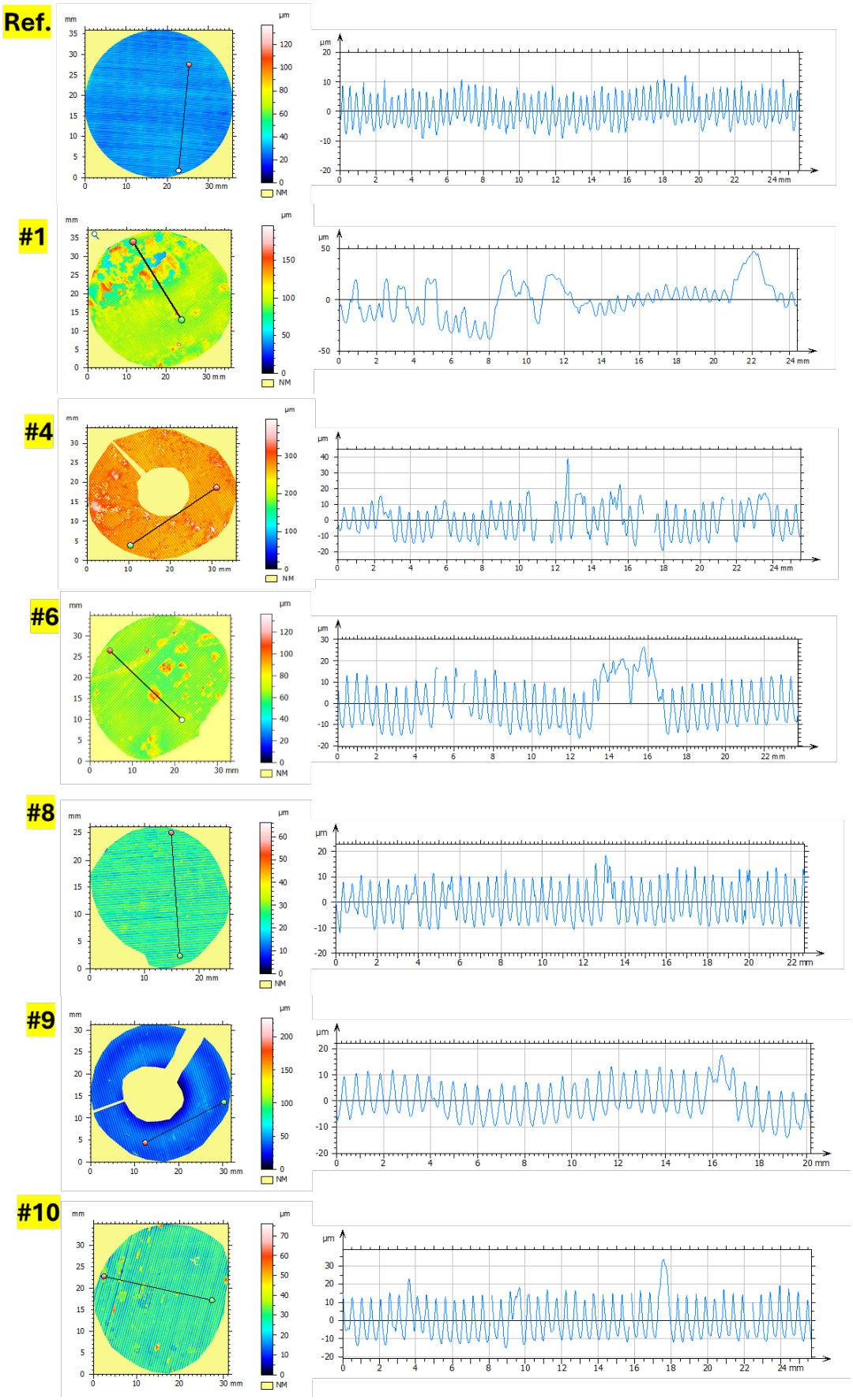

Figure F-2. *Topographic surface profiles (left) and line profiles (right) on the as-received exposed samples and one reference sample.*

Appendix G

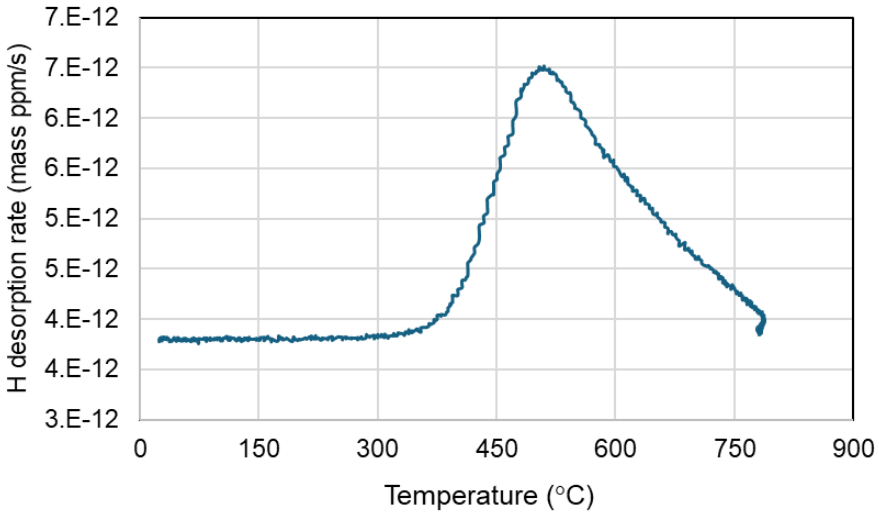

Figure G-1. *TDS curve of sample 8.*

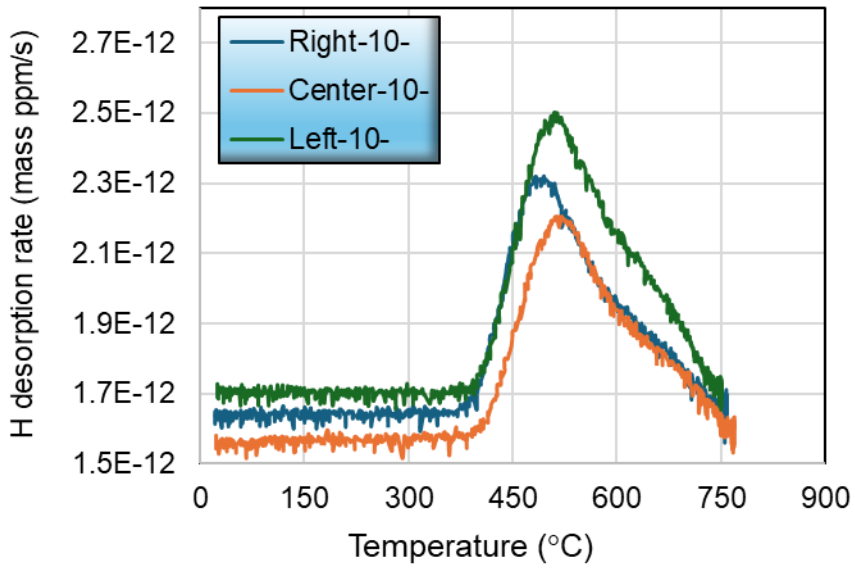

Figure G-2. *TDS curve of sample 10 at different locations.*